Quantized topological energy pumping and Weyl points in Floquet synthetic dimensions with a driven-dissipative photonic molecule

Sashank Kaushik Sridhar,[1] Sayan Ghosh,[2] Dhruv Srinivasan,[1] Alexander R. Miller,[1] and Avik Dutt[1,3,4,*]

[1] *Department of Mechanical Engineering, University of Maryland, College Park, Maryland 20742, USA*
[2] *Department of Physical Sciences, Indian Institute of Science Education and Research Kolkata, Mohanpur, West Bengal 741246, India*
[3] *Institute for Physical Science and Technology, University of Maryland, College Park, Maryland 20742, USA*
[4] *National Quantum Laboratory (QLab) at Maryland, College Park, Maryland 20742, USA*

(Dated: December 7, 2023)

Topological effects manifest in a wide range of physical systems, such as solid crystals, acoustic waves, photonic materials and cold atoms. These effects are characterized by 'topological invariants' which are typically integer-valued, and lead to robust quantized channels of transport in space, time, and other degrees of freedom. The temporal channel, in particular, allows one to achieve higher-dimensional topological effects, by driving the system with multiple incommensurate frequencies. However, dissipation is generally detrimental to such topological effects, particularly when the systems consist of quantum spins or qubits. Here we introduce a photonic molecule subjected to multiple RF/optical drives and dissipation as a promising candidate system to observe quantized transport along Floquet synthetic dimensions, and provide preliminary experiments contrasting the topological and trivial phases. Topological energy pumping in the incommensurately modulated photonic molecule is enhanced by the driven-dissipative nature of our platform. Furthermore, we provide a path to realizing Weyl points and measuring the Berry curvature emanating from these reciprocal-space (k-space) magnetic monopoles, illustrating the capabilities for higher-dimensional topological Hamiltonian simulation in this platform. Our approach enables direct k-space engineering of a wide variety of Hamiltonians using modulation bandwidths that are well below the free-spectral range (FSR) of integrated photonic cavities.

Quantized transport is a hallmark of topological insulators (TIs). Initially explored for electronic transport in condensed matter systems (i.e. quantized Hall conductance [1, 2], Hamiltonians supporting nontrivial topology have now been experimentally simulated in a wide variety of systems such as ultracold atoms [3, 4], photonics [5], acoustics [6, 7] and topolectrical circuits [8]. In such simulators, the Hamiltonians are typically created by controlling the coupling between a lattice of real-space sites encoded, for example, in large arrays of atoms, photonic resonators or photonic waveguides [9–11]. Experiments have reported robust unidirectional edge states [9, 12, 13] in these real-space emulators, but the theoretical and experimental evidence for *quantized* topological transport in photonic TIs remains scant – especially when compared to the near-perfect quantized conductivity [2] in electronic quantum Hall systems to one part in 10^9, which was later used to define the resistance standard [14]. A prime reason for this is the difficulty in defining transport properties and the analog of conductivity for neutral particles such as atoms or photons as they do not naturally respond to electromagnetic fields. Other impediments to ideal transport quantization in real-space simulators include the inescapable effects of dissipation and external driving [15].

In recent years, the concept of synthetic dimensions has emerged by repurposing internal degrees of freedom of atoms and photons as extra dimensions, thus realizing high-dimensional topological phenomena on compact, low-dimensional physical structures [16, 17]. Synthetic dimensions have enabled lattice Hamiltonians with straightforward reconfigurability and tunability, long-range coupling, and artificial magnetic gauge fields for neutral particles, through precise control of coupling between modes labeled by degrees of freedom such as frequency, temporal modes, orbital angular momentum, spin and transverse spatial modes [18–30]. Photonic synthetic *frequency* dimensions, in particular, have successfully demonstrated both Hermitian and non-Hermitian topology, electromagnetic gauge fields, unidirectional edge states, Bloch oscillations, and bulk as well as boundary phenomena [16, 18, 22, 31–37]. However, the aforementioned limitations of *quantized* topological transport in real-space photonic emulators – that of neutral particle transport in electromagnetic fields, the presence of dissipation and drive – also apply to synthetic-space systems.

Here we show how the effects of multiple drives and dissipation can support quantized topological transport of photons, by using the concept of Floquet synthetic dimensions in a pair of modulated cavities, and construct a preliminary experiment to probe for qualitative differences between the topological and trivial regimes. Our system consists of two identical coupled photonic cavities, often called a "photonic molecule" [38, 39], that are modulated to induce transitions between their symmetric and antisymmetric supermodes. This modulation is itself driven by two or more drives at incommensurate frequencies, each of which realizes an orthogonal synthetic di-

* avikdutt@umd.edu

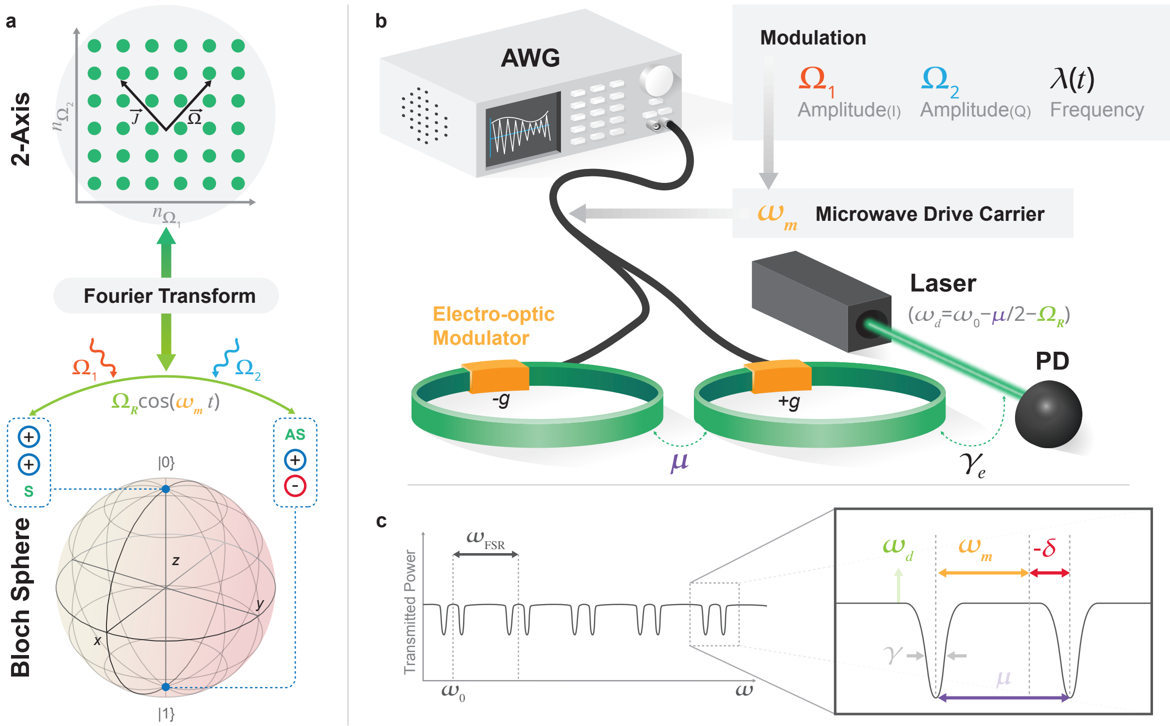

FIG. 1. Schematic of the proposed system. **a.** The non-degenerate eigenmodes separated by the coupling rate μ of the photonic molecule are the symmetric (S) and anti-symmetric (AS) supermodes, i.e., single-ring azimuthal modes that are in-phase (S) or π-phase separated (AS). Coherent evolution in the subspace of a single pair of these resonance modes can be equated to the motion on a Bloch sphere, which is controlled by driving the electro-optic modulator (EOM) with an RF signal nearly resonant with μ ($\omega_m = \mu + \delta$, see inset in **c**). **b.** Proposed setup to create the 2D Floquet lattice of **a** using an RF signal with amplitude I-Q modulation (Ω_1, Ω_2 and frequency modulation $\lambda(t)$ (Eq. (5)). AWG: arbitrary waveform generator. As an example, we can implement the half-BHZ Hamiltonian on a Floquet lattice [Eq. (1)]. Our driven-dissipative protocol also includes an optical laser drive at detuning ω_d and a loss rate γ. **c.** Transmitted power for the setup in **b** without any RF drive on the EOMs.

mension. We refer to the lattice sites created by each incommensurate drive as being along a "Floquet" synthetic dimension. We explicitly construct a 2D Chern insulator that exhibits quantized topological energy pumping, by realizing a driven-dissipative analog of the conservative protocol by Martin, Refael and Halperin [40]. The rate of energy pumping not only survives the effects of external laser drive but is abetted by the presence of finite dissipation. Moreover, the driven-dissipative nature of our protocol obviates the limitations imposed by finite qubit coherence times and the need for complicated state initialization in qubit platforms [41, 42], with the qualitative differences observed in a lossy fiber-optic experiment attesting to the remarkable topological robustness of the 2D Chern TI.

Note that our usage of the term Floquet dimensions distinguishes it from synthetic frequency dimensions although both require modulated photonic cavities, as the modulation frequencies in the former case are significantly below the modulation at the free-spectral-range (FSR) required in the latter case. This eases on-chip realization of our approach in integrated photonics by reducing the demanding bandwidths of low-loss electro-optic modulation. The reduction is particularly beneficial for the photonic construction of high-dimensional models as that would require modulation with frequencies 10-100$\times$ the FSR in the synthetic frequency dimension case.

As an illustration of high-dimensional topology, we use our effectively 0D system to construct a three-dimensional (3D) topological Hamiltonian supporting Weyl points, which act as magnetic monopoles in the reciprocal (k) space of the Floquet lattice [43]. To observe this monopole behaviour, we require a reconstruction of the Berry curvature's 'field' lines, measured around these Weyl points. We conclude by showing how the Berry curvature can be experimentally measured throughout the bands for any general two-band Hamiltonian.

More generally, harnessing Floquet synthetic dimensions offers a powerful tool for direct k-space Hamiltonian engineering in high dimensions using simple, compact geometries with experimentally realizable excitation and measurement protocols.

Half-BHZ model in a photonic molecule and topological energy pumping

To illustrate the analogous topological behavior of temporally modulated systems in Floquet synthetic dimensions, we consider the Bloch form of the Qi-Wu-Zhang model [44] (equivalently, the half–Bernevig-Hughes-Zhang (half-BHZ) model). When implemented on a Floquet lattice by driving a spin (or a two-level system) with two incommensurate (irrationally related) frequencies [40], the Hamiltonian is

$$\begin{aligned}\mathcal{H} = \Omega_R[&\sin(\Omega_1 t + \phi_1)\sigma_x + \sin(\Omega_2 t + \phi_2)\sigma_y \\ &+ \{m - \cos(\Omega_1 t + \phi_1) - \cos(\Omega_2 t + \phi_2)\}\sigma_z]\end{aligned} \quad (1)$$

where $\Omega_1 t + \phi_1 \to k_x$ and $\Omega_2 t + \phi_2 \to k_y$ give us the $\vec{k}$-space representation of the half-BHZ model on a real lattice [45]. This duality between the drive phases and Bloch quasimomentum $\mathbf{k}$ also implies that the linear evolution of the phase with time emulates the effect of a charge moving under an electric field in a 2D lattice. The half-BHZ Hamiltonian breaks both time-reversal and chiral symmetries but possesses particle-hole symmetry with $\hat{C} = \sigma_x K$ and inversion symmetry with $\hat{P} = \sigma_z$, $\hat{C}\mathcal{H}(k)\hat{C}^{-1} = -\mathcal{H}(-k)$ and $\hat{P}\mathcal{H}(k)\hat{P}^{-1} = \mathcal{H}(-k)$. Thus $\mathcal{H}(\vec{k})$ belongs to class D in Altland-Zirnbauer's tenfold way of classification of TIs, and supports chiral transport [46, 47] . It models the behavior of a 2D Chern insulator with a Chern number (C) determined by the value of m; for $|m| > 2$ (trivial phase), $C = 0$, and for $|m| < 2$ (topological phase), $C = 1$. These Chern insulators exhibit an anomalous current that is proportional to C, and the current flows perpendicular to the applied field $\vec{\Omega}$.

Quantized chiral transport is advantageous to probe in Floquet synthetic dimensions as the effective electric field naturally arises here [40], while other real-space and synthetic-space systems with neutral particles require effective electric fields to be explicitly introduced. On the Floquet lattice, this leads to topological energy pumping that is quantized by C, and we therefore expect to see quantized energy transfer from one incommensurate drive to the other. While implementing this Hamiltonian with qubits [41, 42] can produce exotic phenomena such as engineering cat states [48] and quantum state boosting [49], they encounter constraints in demonstrating topological pumping on long timescales due to decoherence. However, barring quantum measurements, this Hamiltonian can be simulated by classical systems, such as magnetic nanoparticles in a time-dependent magnetic field, which allows for a demonstration of topological energy pumping that is unimpeded by the coherence times of qubits. We now look at how a photonic molecule driven by two incommensurate frequencies can implement the same physics encapsulated by Eq. (1).

A photonic molecule comprises two identical optical ring resonators evanescently coupled at a rate μ. [38, 39]. The eigenmodes of the molecule are the symmetric (S) and anti-symmetric (AS) supermodes of various azimuthal orders as shown in Fig. 1. Each ring has an electro-optic phase modulator (EOM) that couples the eigenmodes when driven near the splitting, i.e., $\omega_m \simeq \mu$, with opposite polarities of the RF drive signal $V(t)$. We isolate a single pair of eigenmodes as our two-level system, and work in the single-photon subspace. Taking the bosonic annihilation operators for the uncoupled modes of the two rings to be a_1 and a_2 respectively, we define the S and AS eigenmode annihilation operators as $c_1 = \frac{1}{\sqrt{2}}(a_1 + a_2)$ and $c_2 = \frac{1}{\sqrt{2}}(a_1 - a_2)$, giving us the Hamiltonian,

$$\mathcal{H} = \omega_+ c_1^\dagger c_1 + \omega_- c_2^\dagger c_2 + gV(t)(c_1^\dagger c_2 + c_2^\dagger c_1) \quad (2)$$

where g is the electro-optic coupling strength. Measuring all frequencies relative to the uncoupled ring resonance frequency ω_0, we set $\omega_\pm = \pm\frac{\mu}{2}$. In this single-photon supermode subspace (which is equivalent to coherent state dynamics between the two supermodes), the Pauli operators are defined as usual: $\sigma_x = c_1^\dagger c_2 + c_2^\dagger c_1$, $i\sigma_y = c_1^\dagger c_2 - c_2^\dagger c_1$, $\sigma_z = c_1^\dagger c_1 - c_2^\dagger c_2$, giving us the Hamiltonian

$$\mathcal{H} = -\sigma_z\,\mu/2 + \sigma_x\, gV(t) \quad (3)$$

We now consider a specific form of $V(t)$ as an RF carrier at ω_m with I-Q amplitude modulations (AM) $V_x(t)$ and $V_y(t)$ respectively, as well as frequency modulation (FM) $\lambda(t) = \mathrm{d}/\mathrm{d}t[\Delta(t)]$, leading to,

$$\mathcal{H} = \sigma_z\mu/2 + \sigma_x g\mathrm{Re}\left[\{V_x - iV_y\} \times \exp\{i\omega_m t + i\Delta(t)\}\right]$$

where $\Delta(t) = \int^t \lambda(t')\mathrm{d}t'$. Taking the interaction picture with $|gV(t)| \ll \mu\,\forall\, t$ (weak driving), the effective Hamiltonian under the rotating-wave approximation is (Supp. I),

$$\mathcal{H} = -\frac{\delta + \lambda(t)}{2}\sigma_z + \frac{gV_x(t)}{2}\sigma_x + \frac{gV_y(t)}{2}\sigma_y \quad (4)$$

where $\delta = \omega_m - \mu$. Comparing with Eq. (1) gives us the necessary amplitude and frequency modulation signals to be applied

$$\begin{aligned}\lambda(t) &= gV_0\{\cos(\Omega_1 t + \phi_1) + \cos(\Omega_2 t + \phi_2)\} \\ V_x(t) &= V_0 \sin(\Omega_1 t + \phi_1) \\ V_y(t) &= V_0 \sin(\Omega_2 t + \phi_2)\end{aligned} \quad (5)$$

where $\Omega_R = gV_0/2$. The tunable topological parameter $m = -\delta/(gV_0)$ is now the normalized detuning of the RF drive ω_m from the resonance of the two-level system and maps to a static σ_z coefficient in Eq. (1). Thus, ω_m can be readily controlled from $0 < m < 2$ to $m > 2$ to engender a topological phase transition. The I-Q amplitude modulation maps to σ_x and σ_y components, whereas the frequency modulation maps to the σ_z component.

Note that this system can be made to evolve adiabatically, i.e., $\Omega_1, \Omega_2 \ll gV_0$, by choosing the frequency scales of our modulation accordingly. We also emphasize that all frequency scales in our proposed implementation are much below the ring's free-spectral range

($\Omega_1, \Omega_2 \ll \mu \ll \omega_{\rm FSR}$), thus easing bandwidth requirements for integrated photonic modulators. Thus, we have showed how the 2D half-BHZ Hamiltonian can be realized in a photonic molecule, an effectively 0D system, with appropriately engineered drives and detunings, but in an as-of-yet conservative system. We remark that higher-order topology has been proposed to be realizable in 1D and 2D arrays of modulated ring resonators [50], but they are subject to the same constraint of FSR modulation, limiting their scaling. Before introducing dissipation and external drive, we briefly summarize the phenomenon of quantized topological energy pumping as introduced in [40]. Splitting the Hamiltonian into the respective Ω_1 and Ω_2 drive contributions:

$$\mathcal{H} = h_1(t) + h_2(t) + \sigma_z\,\delta/2, \tag{6}$$

the work done by each drive $i = 1, 2$ over time T is given by

$$W_i(T) = \int_0^T dt \left\langle \frac{dh_i}{dt} \right\rangle \tag{7}$$

For Ω_1/Ω_2 irrational, the system samples the full Brillouin zone, leading to quantized energy pumping:

$$W_1 = -W_2 = C\frac{\Omega_1\Omega_2 T}{2\pi} \tag{8}$$

where C is the Chern number.

Driven-dissipative quantized pumping in a photonic molecule

We next explore how the addition of an external laser drive and cavity dissipation enable quantized topological energy pumping in a quasi-steady state regime without stringent requirements on initialization of the molecule's state. Dissipation is natural as all optical ring resonators have finite Q-factors, which define the photon decay rate γ for the system. Nevertheless, this decay affects both modes symmetrically, and they can be renormalized to look at the dynamics within the two-level subspace. This is a unique advantage that photonic systems provide, and motivates us to verify persistent topological pumping when adding an external optical drive. The driven-dissipative equations of motion for c_1 and c_2 are

$$\dot{c}_{1,2} = i[\mathcal{H}, c_{1,2}] - \gamma c_{1,2} + \sqrt{\gamma_e}s_{in}(t)e^{\pm i((\mu+\delta)t+\Delta(t))/2} \tag{9}$$

where γ_e is the coupling rate into the bus waveguide, and $s_{in}(t)$ is the external laser drive (note that from this point onward in the text, we distinguish between the Hamiltonian drives Ω_1 and Ω_2 and the external optical/laser drive $s_{in}(t)$). We physically motivate the chosen laser frequency when discussing the 2D density of states in the latter part of the paper, where we look at the adiabatically varying eigenspectrum of the Hamiltonian in Eq. (4), as a function of m.

Topological signatures in temporal and spectral dynamics

This system shows a variety of topological signatures even with drive and dissipation added into the mix [Fig. 2], reinforcing the remarkable robust topology of the conservative half-BHZ model. In Fig. 2(a), a clear qualitative difference is seen in the spectral amplitudes of one of the super-modes (denoted by c_1): The topological regime is characterized by a dense spectrum with a continuous floor, indicative of the aperiodic evolution of the system, while the trivial regime shows several discrete peaks that represents the periodic localization in the dynamics. Our numerical simulations reproduce results calculated in a conservative system averaged over initial states [51]. Note that no such averaging over initial states is required in our model, as the signatures presented are long-time quasi-steady-state simulations; they are fairly independent of the initial state transients which have decayed at long times.

As noted previously, the hallmark of this Hamiltonian is the presence of quantized topological pumping, which is absent in the trivial regime. In Fig. 2(b), we see that the work done by the Ω_1 drive (W_1) increases at the quantized rate stated in Eq. (8), while the Ω_2 drive (W_2) decreases correspondingly, reflecting that there is energy being pumped from one drive to the other. The linear slopes reinforce the quantization by the Chern number C, with the pumping rate being 1.022 and -1.010 for W_1 and W_2 respectively in the topological phase (top figure) and correspondingly -0.053 and 0.070 in the trivial phase (bottom). The Bloch sphere plots (Fig. 2(b) insets, SI video 1 and SI video 2) reflect the ergodic behavior of the system in the topological regime, while the trivial regime dynamics remains localised near the $|0\rangle$ state. Remarkably, we are not limited by the photon lifetime ($\tau_p = 1/\gamma$, with $\gamma \approx 0.01\Omega_1/\pi$), and see sustained pumping for ~ 5 photon lifetimes for $m = 1$. Almost no pumping is observed for $m = 3$ in the trivial regime. An important detail here is that the pumping is being observed under a quasi-steady state condition, due to the drive and dissipation, thus obviating the need for complicated Floquet eigenstate initialization in previous protocols [41, 42] and allowing us to start with vacuum states in both resonators.

One way to verify the need for incommensurateness in the Hamiltonian's drive frequencies is to observe the dynamics for rational values of $\Omega_1/\Omega_2 = p/q,\ p, q \in \mathbb{Z}$. We see the absence of a transition in this case, as the half-BHZ model effectively becomes a 1D tight-binding Hamiltonian with long-range couplings [18, 52, 53]. The pumping rate no longer depends on the Chern number C, but on the integrated Berry curvature over specific periodic trajectories in the Brillouin Zone. We therefore also see periodic orbits on the Bloch sphere (SI video 3 and SI video 4).

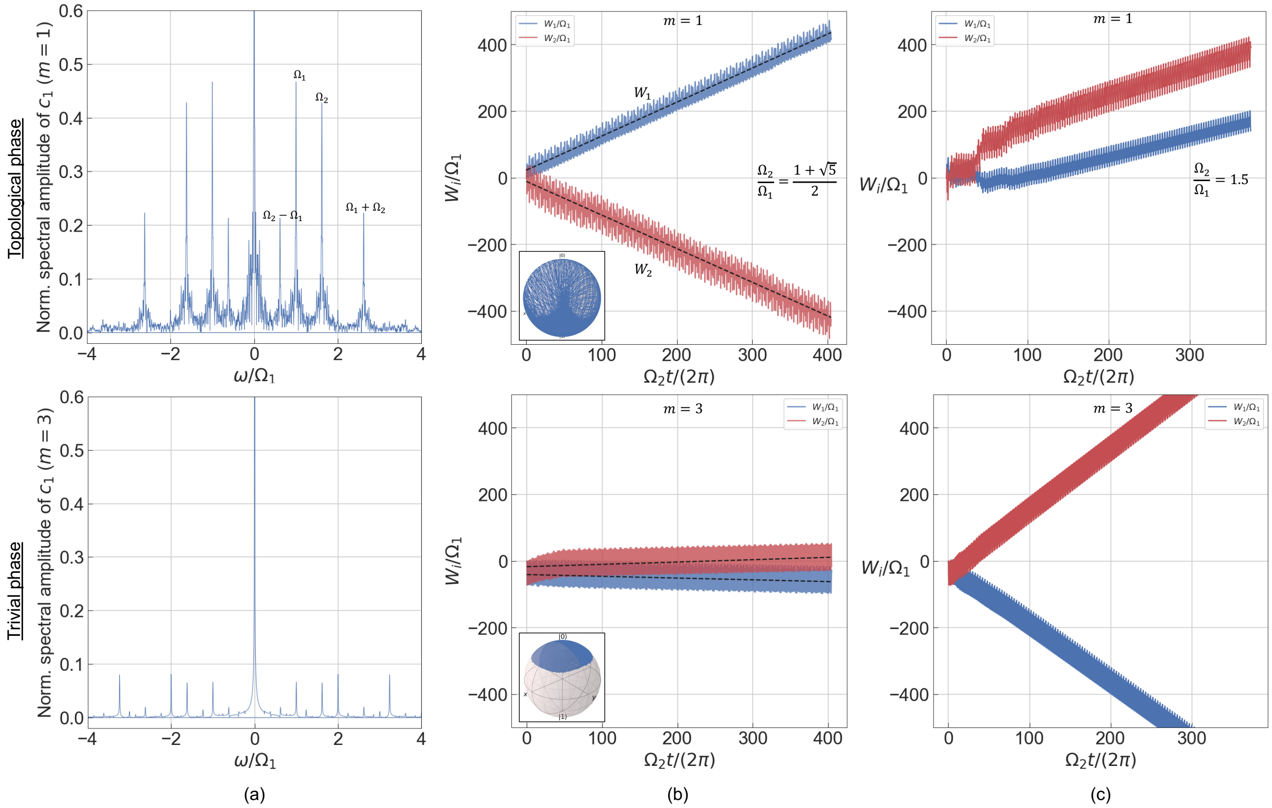

FIG. 2. Spectral and temporal signatures of topological dynamics, in the presence of optical drive and dissipation. (a) Normalized spectral amplitude of the symmetric super-mode c_1. In the topological regime ($m = 1$) we see the dense spectrum showing a continuous floor, indicative of aperiodic and highly delocalized dynamics that are characterized by harmonics of the incommensurate drives, Ω_1 and Ω_2. In the trivial regime ($m = 3$), the spectrum is discrete with sharp peaks, indicating periodic orbits and localization in the Bloch sphere. (b) Normalized work done by the drives Ω_1 and Ω_2 in the topological ($m = 1$) and trivial ($m = 3$) regimes. W_1 and W_2 respectively show slopes of 1.022 and -1.010 in the topological regime over ~ 5 photon lifetimes, and almost no pumping (slopes of -0.053 and 0.070 respectively for W_1 and W_2) in the trivial regime, clearly exhibiting the linear dependence on the Chern number C. Insets show Bloch sphere trajectories. (c) Dynamics for commensurate drives ($\Omega_2/\Omega_1 = 1.5$) shows no quantization and the possibility of higher pumping rates in the trivial regime (see text).

Impact of dissipation on topological pumping

A unique feature of our system is the interplay between the dynamics and the dissipation. We show in Fig. 3 that the topological pumping loses quantization for higher values of γ, but the striking qualitative contrast between the topological and trivial regimes still persists up to $\gamma > \Omega_1, \Omega_2$. Although the normalized pumping rate seems to increase, the total power $|c_1|^2 + |c_2|^2$ reduces on average in the new quasi-steady state, leading to a net reduction in pump power. Physical intuition for the loss of pumping beyond a certain $\gamma \gg 10\Omega_1/\pi$ comes from the coupled oscillator system becoming over-damped, washing out the topological dynamics and the pumping effects.

Experimental feasibility and preliminary experimental data

The concept of a photonic molecule offers a sufficiently mature platform to implement driven-dissipative topological energy pumping, as evidenced by its potential utility in various other fields, such as spectral engineering in photonic biosensors [54], dissipative soliton Kerr combs [55], squeezed light generation [56, 57], optomechanics [58], microlasers [59], and dynamically-controlled photonic memories [39]. Using electro-optically modulated ring resonators in thin-film lithium niobate (TFLN), or piezo-electric aluminium nitride actuators [60], one can envision an artificial spin that can implement time-dependent spin Hamiltonians with sub-FSR modulation.

State-of-the-art TFLN resonators have demonstrated loaded Q-factors of $\sim 10^7$ [61], and photonic molecule mode splittings of around $\mu = 7$ GHz [39], but can potentially be even higher by reducing the spacing between

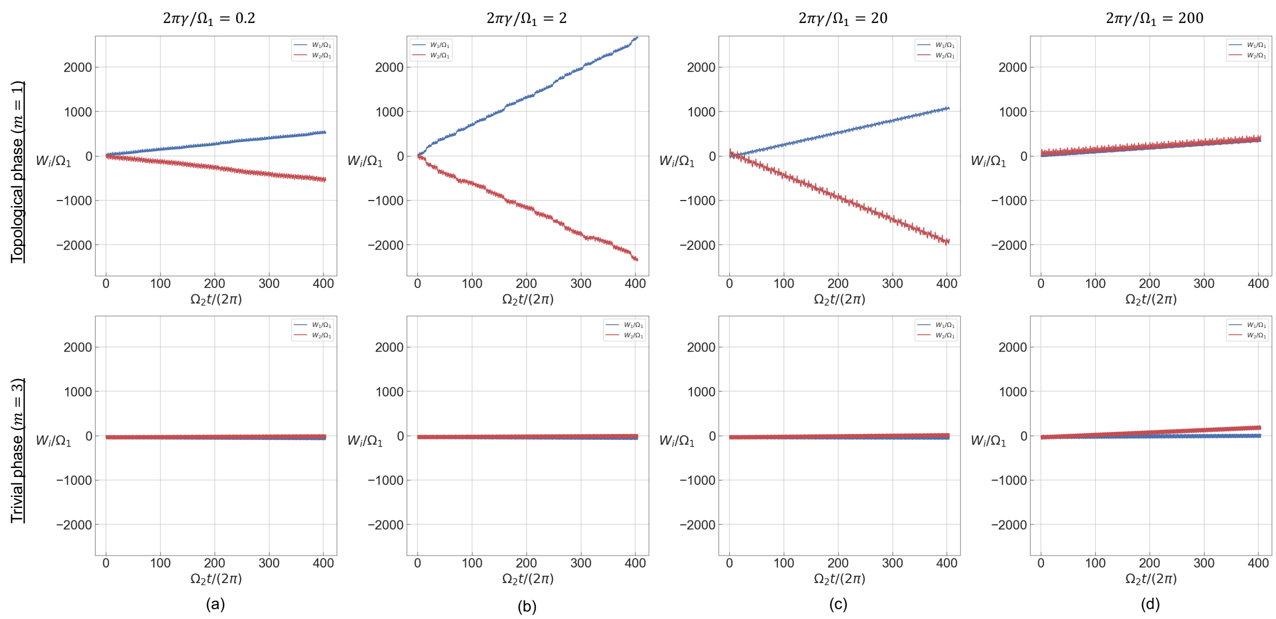

FIG. 3. Work done by the drives, simulated for $\gamma =$ (a) $0.1\Omega_1/\pi$, (b) Ω_1/π, (c) $10\Omega_1/\pi$, and (d)$100\Omega_1/\pi$. We see close to quantized pumping in (a) with slopes of 1.261 and -1.342 for W_1 and W_2 respectively, which increases and starts to disappear in (b) and (c). Almost no observable phase transition behavior occurs in (d), due to overdamped oscillator dynamics. The increase in slope is not an anomaly, however, as the actual work done, without normalization depends on $|c_1|^2 + |c_2|^2$, which reduces by orders of magnitude and kills the effect of the increased slope (Supp. Fig. S3) .

the rings or increasing the coupling lengths. Such a 3-4 orders-of-magnitude frequency separation between μ and γ demonstrates the feasibility of adiabaticity and observing longer time evolution in these near-term devices, under practical frequency and loss constraints. As a concrete example system, we envision the following implementation: A photonic molecule consisting of coupled lithium niobate ring resonators, with bus waveguides coupling light in and out of both rings. An FSR of $\sim$ 250GHz can be achieved with a loaded $Q \sim 10^7$ at the telecom C-band (1550nm) [62]. A splitting $\mu \sim$ 50GHz is attainable by suitably designing the coupling length and gap between the rings. The frequency Ω_R in Eq. (1) corresponds to the Rabi oscillation frequency of the qubit/spin. In the photonic molecule, this is directly proportional to the peak RF voltage driving the EOMs, and the electro-optic efficiency g. For $g \sim 0.5 - 1$ GHz/V, in line with [63], one can achieve $\Omega_R \sim 2.5$ GHz with peak voltage $V_0 \sim 5-10$V. This sets the RF drive frequency $\omega_m = \mu - mgV_0$ to lie in the range $35 - 45$ GHz for probing the system at $1 < m < 3$. To match the adiabaticity condition from our simulations, one can set $\Omega_1, \Omega_2 \sim 125$ MHz, which is sufficiently larger than the photon loss rate from the photonic molecule of $\sim$ 20MHz. All of the experimental parameters stated can be achieved realistically in an on-chip platform [62, 64]

This sets the photonic molecule system apart from prior implementations with quantum spins such as NV-centers [41] and superconducting qubits [42]. Quantum noise and decoherence in quantum spins limit the operation times, necessitating quantum error-correction to recreate the expected dynamics [42]. Moreover, limits on engineering level-splittings make adiabatic operation quite difficult, necessitating counterdiabatic drives [65] which further complicate the RF signal-engineering requirements. While classical spins such as magnetic nanoparticles, as suggested by [40], offer some mitigation, the spatially complex experimental setups with 3D control of the magnetic fields experienced by these nanoparticles could be challenging. Moreover, a driven-dissipative implementation such as the one proposed here would be non-trivial to realize. These issues are circumvented by the modulated photonic molecule, which encodes all three spin terms of the Hamiltonian in the three different signal-modulation degrees of freedom (in-phase, quadrature, and frequency), along with the ability to operate the system in a driven-dissipative quasi-steady state by simply adding an external bus waveguide coupled to a continuous-wave laser source.

To investigate the predictions of our Floquet synthetic dimension-based protocol qualitatively, we employ a fiber-based photonic molecule setup along the lines of Refs. [36, 66], the schematic of which can be found in Supp. Fig. S7. Through independent calibrations, we measure the FSR of the rings, the supermode splitting, and the linewidth to be $\omega_{FSR}/2\pi = 36.5$ MHz, $\mu/2\pi = 6.08$ MHz, and $\gamma/2\pi = 0.83$ kHz respectively. Fig. 4(a) shows the transmission spectrum of the constructed photonic molecule, as illustrated in Fig. 1. One may notice that $\mu/\gamma \sim 7$ is significantly smaller than

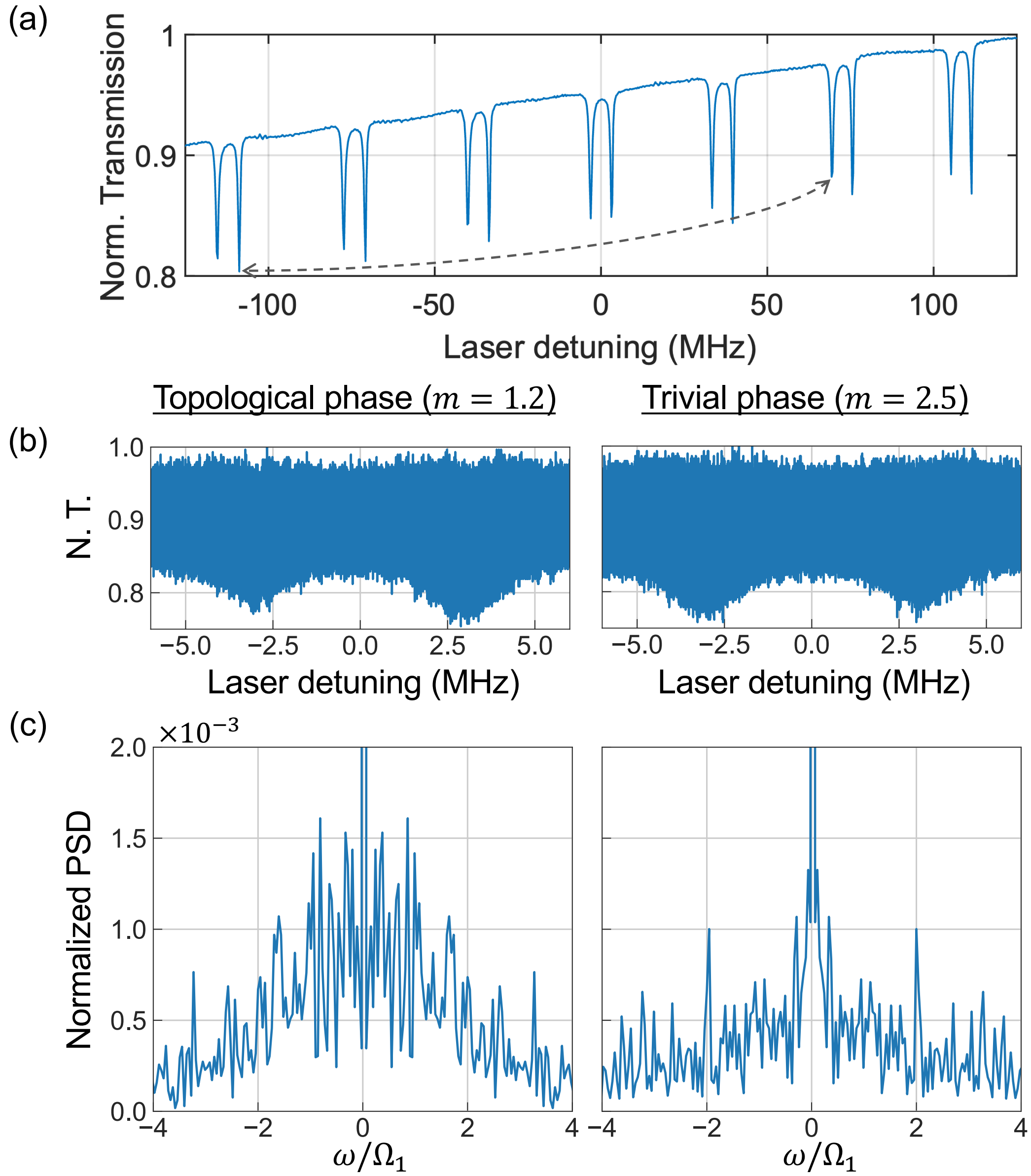

FIG. 4. Experimental data from a fiber-based photonic molecule. (a) Normalized Transmission spectrum of the photonic molecule, with $\omega_{FSR} \sim 36.5$MHz, $\mu \sim 6.08$MHz, and $\gamma \sim 0.83$kHz. Due to μ/γ being much smaller than the proposed regime, modulation is done between conjugate supermodes five FSRs away, i.e., $\mu_{new} = 5\omega_{FSR} - \mu = 176.42$MHz. (b) Normalized transmission (N. T.) after adding modulation from the AWG. The laser sweep shows dense modulation of the supermode spectra, but no discernible difference between the two regimes. (c) Normalized power spectral density, calculated using a sample of data around the laser detuning limited by the AWG period. The topological regime shows a denser spectrum, with clustered peaks and a raised, continuous noise floor, while the trivial regime shows a sparser spectrum and no raised noise floor, in agreement with the simulations in Fig. S8 and [51].

the requirements cited for the on-chip implementation ($\mu/\gamma \sim 2500$), with the losses drowning out the signatures of the topological pumping. To alleviate this mismatch of regimes, we choose two opposite-parity supermodes belonging to different azimuthal order resonances of the rings to form the two-level system. These two modes are separated by $\mu_{new} = 5\omega_{FSR} - \mu = 2\pi \cdot 176.42$ MHz. The RF modulation has a carrier ω_m near this frequency to achieve a larger effective $\mu_{new}/\gamma \sim 210$ and better observe the qualitative signatures of topology. After further calibrating the modulators to obtain the modulation strength gV_0, the AWG is programmed to generate the required signal. With the goal of observing a qualitative difference across the topological transition by leveraging a direct transmission measurement, we attempt to measure the spectral signatures posited

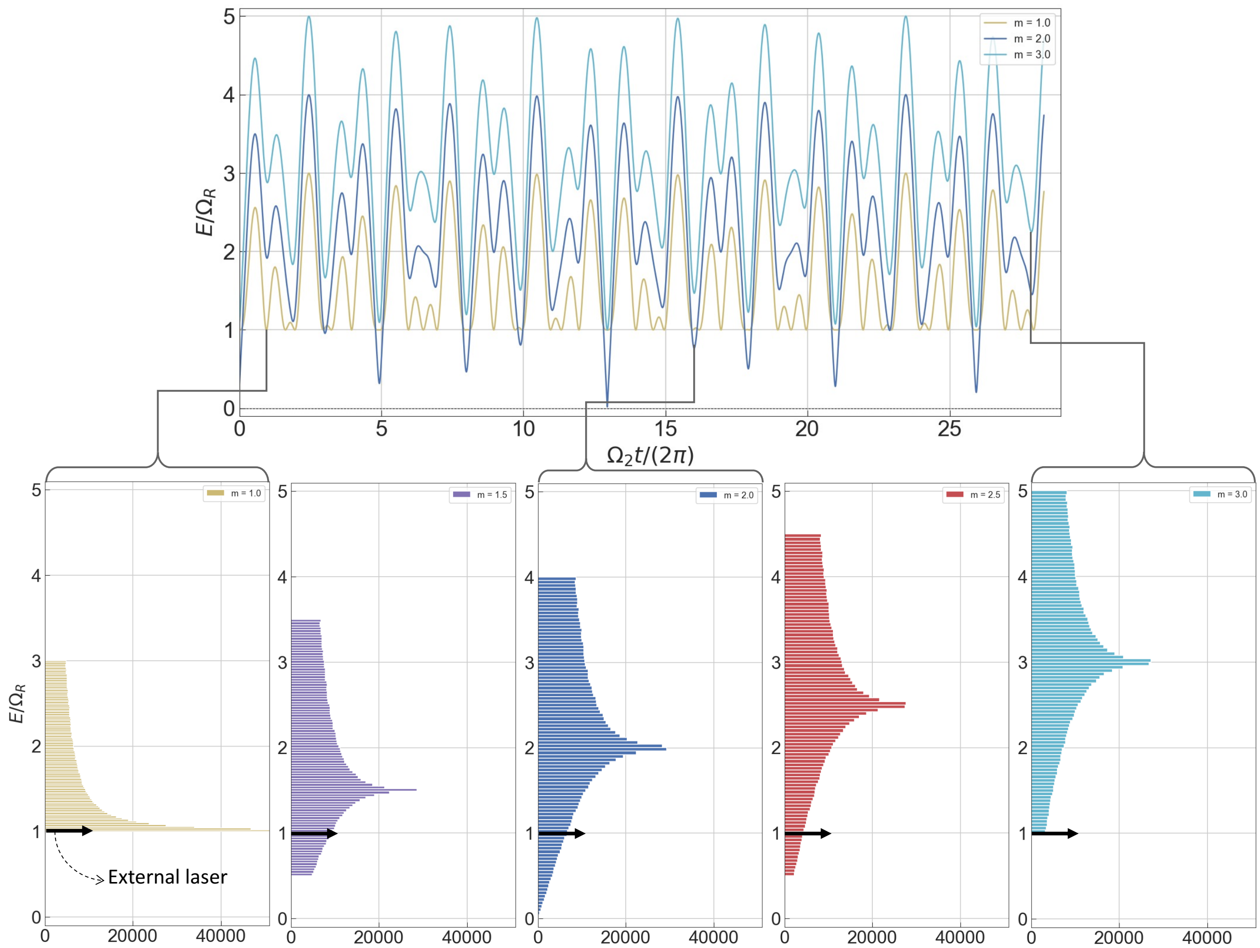

FIG. 5. Adiabatically varying eigenenergy of $\mathcal{H}$ and the Density of States (DoS). The top figure shows the normalized eigenenergy varying with time for $m = 1$, 2 and 3, plotted for initial phases $\phi_1 = 0$ and $\phi_2 = \pi/10$. A smaller time interval of the full simulation is shown to lucidly show the quasi-periodic evolution. The bottom figures show histograms generated over the full time evolution, for more values of m, showing the closing of the gap at $m = 2$. The chosen detuning of the laser at $\omega_d = \Omega_R$ is marked in all the histograms, and we see a non-zero DoS here for $1 \leq m \leq 3$.

in Fig. 2(a). Fig. 4(b) shows the modulated photonic molecule's transmission spectrum. Despite the transmission not showing any apparent differences between the two regimes, taking a Fourier transform of the samples near the requisite laser detunings results in qualitatively different spectra in the topological and trivial regimes, as evidenced by Fig. 4(c). While the topological spectrum is dense and shows a continuous noise floor, the trivial regime shows a sparser spectrum and more spaced out peaks at the characteristic driving frequencies, providing evidence of the existence of driven-dissipative topological dynamics (see Fig. 2(a) and [51]). Although these measurements do not accurately reflect the simulations in Fig. 2(a) due to the difference in the proposed parameters and what is implemented in the fiber experiment, they agree well with simulations performed with the same parameters and same number of samples (see Fig. S8 in the supplement). It is therefore worth noting that although this is noticeably far from the frequency regimes proposed for the on-chip implementation, we still see signatures of topological behaviour that survive and are reasonably robust in a lossy fiber-optic implementation.

While an on-chip implementation can, in principle, achieve the parameters at the beginning of this section and in Fig. 2 and Fig. 3, simultaneous realization of efficient modulation, large bandwidth, and low loss in a ring resonator with FSR$\sim$ 1 THz lie at the threshold of what is possible with state-of-the-art TFLN nanophotonics. In the interim, one could implement the workaround used in the fiber experiment - coupling opposite-parity supermodes that are not separated by μ, but further apart at $\omega_{FSR} - \mu$ for instance. This alleviates the THz-range FSR requirement and allows for the use of racetrack resonators, leading to larger coupling and better efficiency in modulation, while also reducing bending losses. Although this brings back the initial challenge of large-bandwidth modulation, also an issue in synthetic frequency dimension proposals, we show in further sections how the straightforward addition of a third incommensurate frequency can lead to higher-dimensional topology. This is non-trivial to achieve in synthetic frequency lattices, as one possible way to realize it uses longer-range couplings beyond the FSR modulation [34, 53, 67], placing a larger burden on the bandwidth.

While the discussion so far has shown that drive and dissipation in the photonic molecule retain, and possibly even prolong, topological effects, current experimental work has shown that photon lifetimes can be improved enough to see adiabatic dynamics over multiple cycles of the Ω_1 and Ω_2 drives, by fabricating sufficiently high-Q resonators ($Q > 10^8$). We next discuss phenomena that can be explored in the regime where dissipation is minimized, the external laser drive is absent, and state initialization is incorporated, which is yet another capability of the photonic molecule. With this, one can envision directly probing the band structure, density of states (DoS), and even the Berry curvature of two-band Hamiltonians in 2D and higher dimensions, which we discuss over the remainder of this paper.

Measuring 2D band structure and Density of States

The Hamiltonian in Eq. (1) is easily diagonalizable due to its representation as a 2×2 matrix, giving us positive and negative eigenvalues:

$$\begin{aligned} E_+ &= \Omega_R \big[\sin^2(\Omega_1 t + \phi_1) + \sin^2(\Omega_2 t + \phi_2) \\ &\qquad + (m - \cos(\Omega_1 t + \phi_1) - \cos(\Omega_2 t + \phi_2))^2 \big]^{1/2} \\ &= E \\ E_- &= -E \end{aligned} \tag{10}$$

When taking the adiabatic limit, the system's eigenenergies vary slowly relative to Ω_R as seen in Fig. 5. Mapping the time evolved to the phases of the drives, which act as the synthetic lattice momenta of our 2D system, we can map these energies to their respective drive phases and construct the Floquet band structure. Furthermore, sampling the eigenenergies over a long enough time evolution (to ensure ergodicity) and building a histogram of the values it takes, we end up with the density of states (DoS) of this two-band Floquet system.

Examining this system without the external laser drive, if we now include the step of initializing the system to one of the two Floquet eigenstates $|n\rangle$, we can measure $\langle\sigma_x\rangle_n$, $\langle\sigma_y\rangle_n$ and $\langle\sigma_z\rangle_n$ expectation values at all times, as the system remains in this eigenstate due to adiabatic evolution. This allows us to measure $E(t)$ with the following expression:

$$\begin{aligned} E &= \langle\mathcal{H}\rangle_n \\ &= \Omega_R \big[\sin(\Omega_1 t + \phi_1)\langle\sigma_x\rangle_n + \sin(\Omega_2 t + \phi_2)\langle\sigma_y\rangle_n \\ &\qquad + \{m - \cos(\Omega_1 t + \phi_1) - \cos(\Omega_2 t + \phi_2)\}\langle\sigma_z\rangle_n \big] \end{aligned} \tag{11}$$

Mapping t to the phases of both drives allows us to directly measure the band-structure, and taking the histogram also gives us the density of states. Fig. 5 shows these histograms for varying values of m across the topological and trivial regimes, showing a non-zero DoS near $E = 0$ and illustrating the gap closure at the transition point when $m = 2$. We see that for $1 \leq m \leq 3$, the DoS at $E = \Omega_R$ is non-zero, and shows how this point ranges from being a van Hove singularity at $m = 1$, to being at the minimum eigenenergy for $m = 3$. We also see that the DoS reduces in magnitude monotonically in this range of m values.

Although this analysis does not include any external laser driving the system, the DoS allows us to physically motivate the chosen frequency of our external laser drive by assessing how often the laser is driving the system's eigenstates at resonance, thus allowing us to define the ideal detuning for a range of m we would like to probe. When the laser is detuned to $\omega_d = \omega_0 - \mu/2 - \Omega_R$, where ω_0 is the single-ring resonance and μ is the supermode splitting (we rotate these frequencies out in the Hamiltonian), it resonantly drives the photonic molecule's supermode only at the instants of time when $E(t) = \Omega_R$, and the DoS tells us how frequently this occurs. The non-zero DoS at $E = \Omega_R$ across the range $m = 1$ to 3 thus motivates us to detune the laser to this frequency to measure driven-dissipative topological energy pumping.

Scaling to higher dimensions: Weyl points

The key advantage of Floquet synthetic dimensions is the ability to engineer higher-dimensional Hamiltonians, with relatively simple additions to the current setup with a photonic molecule. By simply adding a third incommensurate frequency to the modulation, we can create bulk 3-D non-trivial topology, leading to phenomena such as Weyl points [43]. These points have garnered great interest in the community for the fundamentally unique phenomena they lead to, such as Fermi arc surface states [68], which also hold potential for applications in next-generation electronics [69, 70].

Furthermore, Weyl points behave as monopoles of the Berry curvature (akin to a magnetic field in momentum space), and the Berry curvature surrounding a Weyl point has not been measured experimentally before. In photonics, higher-order (quadratic) Weyl points have been demonstrated in specially-fabricated 3D photonic crystals [71], where the band structure was probed with Fourier-transform infrared spectroscopy. In synthetic lattices, however, we can envision a more direct probe for Weyl points. For completeness, we mention that there are two routes to increasing the dimensionality of the system and obtaining Weyl points - introducing a third incommensurate frequency, or simultaneously harnessing the frequency synthetic dimension of the rings by modulating at the free spectral range [22, 31]. While modulation at ω_{FSR} offers the capability to create boundaries

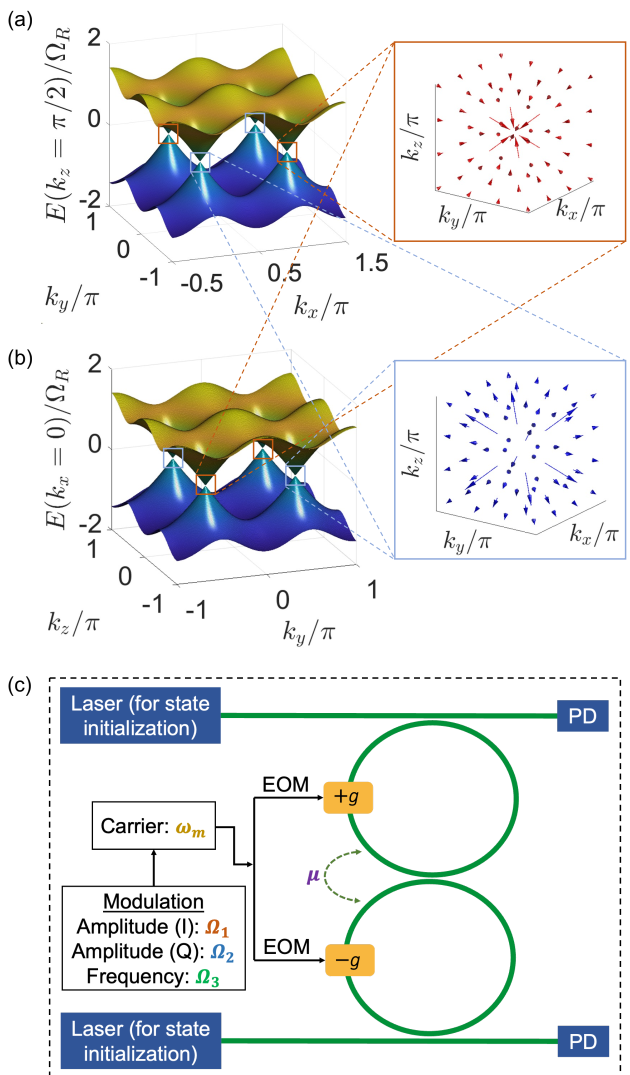

FIG. 6. The band structure for a Weyl point Hamiltonian along the (a) $k_x k_y$-plane, and the (b) $k_y k_z$-plane. The band-touching Weyl points show isotropic linear dispersion in their vicinity, with their topological robustness quantified by the Berry curvature flux normal to a surface near the Weyl point being quantized. Neighbouring Weyl points show opposite signs in the quantized flux, indicated by the insets, which show the Berry curvature field lines in 3-D. This behaviour is indicative of synthetic magnetic field lines originating from a Weyl point and converging at the neighbouring Weyl point, leading to the physical picture of Weyl points as monopoles of the synthetic magnetic field. The experimental schematic to achieve this is shown in (c), where the addition of a third incommensurate frequency in the frequency modulation can lead to three-dimensional topology.

on the frequency lattice [36, 37, 72, 73], adding a third incommensurate frequency gives us the k-space Hamiltonian directly, and so this is the method we focus on in this text. As an example, we can look at Weyl Hamiltonians such as [74]:

$$\mathcal{H}(\mathbf{k}) = \Omega_R\{\sin(k_x)\sigma_x + \cos(k_y)\sigma_y + \cos(k_z)\sigma_z\} \quad (12)$$

The band structure of this Hamiltonian is shown in Fig. 6, where we see linear dispersion in all three directions near the band-touching points at $(0, \pm\pi/2, \pm\pi/2)$ and $(\pi, \pm\pi/2, \pm\pi/2)$. As mentioned previously, the σ_x and σ_y terms can be achieved respectively by in-phase and quadrature amplitude modulation, while the σ_z term comes from frequency modulation of the RF signal. By mapping k_x, k_y and k_z to incommensurate phases $\Omega_1 t + \phi_1$, $\Omega_2 t + \phi_2$ and $\Omega_3 t + \phi_3$ (all three of them are irrationally related), we can achieve quasi-periodic time evolution that emulates the k-space evolution of the Weyl Hamiltonian. As with the 2D case, the experimental constraints lie in how "irrational" the three frequencies are, limited by how precisely the numerical values of the three frequencies can be defined by the instruments. In principle, therefore, there exists a finite time up to which the dynamics is quasi-periodic, but this can be engineered to far exceed the time we probe the system for, which is usually limited by the photon lifetimes of the ring resonators.

What makes our method especially powerful is that we can now experimentally map out the Berry curvature throughout the bands, for any given two-band Hamiltonian $\mathcal{H}(\mathbf{k})$, by tracking the dynamics of the artificial spin encoded in the photonic molecule. This allows us to generate Berry curvature data similar to what the insets in Fig. 6 display in the vicinity of each Weyl point, thus verifying their synthetic monopole character. To buttress this claim, we calculate $\mathbf{B}(\mathbf{k})$ in a gauge-invariant fashion as [75]:

$$\mathbf{B}(\mathbf{k}) = \sum_{m \neq n} \mathrm{Im}\left[\frac{\langle n(\mathbf{k})| \{\nabla_{\mathbf{k}}\mathcal{H}(\mathbf{k})\} |m(\mathbf{k})\rangle \times \langle m(\mathbf{k})| \{\nabla_{\mathbf{k}}\mathcal{H}(\mathbf{k})\} |n(\mathbf{k})\rangle}{(E_m - E_n)^2}\right] \quad (13)$$

where $|m(\mathbf{k})\rangle$ and $|n(\mathbf{k})\rangle$ are the eigenvectors of $\mathcal{H}(\mathbf{k})$, E_m and E_n being the corresponding eigenvalues. Solving for the general eigenvalues and eigenvectors of the 2×2 Hamiltonian (Supp II), this simplifies to

$$\mathbf{B}(\mathbf{k}) = \frac{\Omega_R^2}{4E_m^2}\Bigg[\hat{k}_x \sin(k_y)\sin(k_z)\left(\langle n|\,\sigma_x\,|n\rangle - \frac{\Omega_R \sin(k_x)}{E_m}\right) - \hat{k}_y \cos(k_x)\sin(k_z)\left(\langle n|\,\sigma_y\,|n\rangle - \frac{\Omega_R \cos(k_y)}{E_m}\right) - \hat{k}_z \cos(k_x)\sin(k_y)\left(\langle n|\,\sigma_z\,|n\rangle - \frac{\Omega_R \cos(k_z)}{E_m}\right)\Bigg] \tag{14}$$

With Floquet synthetic dimensions in a photonic molecule, we can envision the following protocol: Initialize to the eigenstate $|n\rangle$ for a given initial phase and drive adiabatically with three incommensurate frequencies, while measuring the spin expectation values for all k except at the Weyl points. Here, the eigenstate flips due to the band-touching, and the Berry curvature diverges, so we can threshold this measurement and accumulate experimental runs over multiple initial phases to reconstruct the insets in Fig. 6. Thus, the photonic molecule can provide a novel experimental probe for the Berry curvature of a topological Floquet system.

Discussion and Outlook

In summary, we have proposed a new candidate system to engineer topological Hamiltonians in a 2-D Floquet synthetic lattice, and have shown that it exhibits topological energy pumping that persists in the presence of dissipation and an external drive, over multiple parameter regimes. The pumping persists over multiple photon lifetimes and stays quantized in the normalized spin subspace. Furthermore, this system can be extended to simulate higher-dimensional Hamiltonians with the straightforward addition of an extra incommensurate frequency. As an example, we look at Weyl points and provide a path forward to observing them in a photonic molecule. While synthetic dimensions offer many advantages by circumventing the complexity of constructing analogous material systems, such as in cold-atom experiments [74], the complexity inherently shifts to the control signal RF engineering requirements. Moreover, measuring the topological pumping requires information about the complex amplitudes of c_1 and c_2, which necessitate dynamically frequency-tuned phase-sensitive detection schemes. Nevertheless, these capabilities can be envisioned, with the added benefit of scalability through photonic integration. With a preliminary demonstration, we have showed that topological behaviour can be qualitatively inferred even from a fiber-optic experiment using spectral measurements. This further consolidates the case for integrated photonics, as on-chip electro-optically modulated ring resonators with quality factors upwards of 10^6, driven by state-of-the-art electronics, have been demonstrated [39, 61]. Amajor step forward lies in the frequencies we modulate at, since $\omega_m \ll \omega_{FSR}$ for Floquet synthetic dimensions, which eases up the specifications on electronics for driving on-chip devices. Extensions of our approach should also support novel processes such as enantioselective topological frequency conversion by incorporating more than two levels in the driven spin [76]. One can thus envision a fully integrated device that can achieve high-dimensional Hamiltonian analog simulation and quantized topological transport in this framework for considerable periods of time.

ACKNOWLEDGEMENTS

This work was supported by a Northrop Grumman seed grant, a National QLab joint seed grant from IonQ and the University of Maryland, and a NSF QuSeC-TAQS grant # 2326792. We thank Chad Smith for Figure 1.

[1] K. v. Klitzing, G. Dorda, and M. Pepper, New Method for High-Accuracy Determination of the Fine-Structure Constant Based on Quantized Hall Resistance, Phys. Rev. Lett. **45**, 494 (1980).
[2] D. J. Thouless, M. Kohmoto, M. P. Nightingale, and M. den Nijs, Quantized Hall Conductance in a Two-Dimensional Periodic Potential, Phys. Rev. Lett. **49**, 405 (1982).
[3] H. Miyake, G. A. Siviloglou, C. J. Kennedy, W. C. Burton, and W. Ketterle, Realizing the harper hamiltonian with laser-assisted tunneling in optical lattices, Phys. Rev. Lett. **111**, 185302 (2013).
[4] M. Aidelsburger, M. Atala, M. Lohse, J. T. Barreiro, B. Paredes, and I. Bloch, Realization of the hofstadter hamiltonian with ultracold atoms in optical lattices, Phys. Rev. Lett. **111**, 185301 (2013).
[5] H. Price, Y. Chong, A. Khanikaev, H. Schomerus, L. J. Maczewsky, M. Kremer, M. Heinrich, A. Szameit, O. Zilberberg, Y. Yang, B. Zhang, A. Alù, R. Thomale, I. Carusotto, P. St-Jean, A. Amo, A. Dutt, L. Yuan, S. Fan, X. Yin, C. Peng, T. Ozawa, and A. Blanco-Redondo, Roadmap on topological photonics, J. Phys. Photonics **4**, 032501 (2022).
[6] A. B. Khanikaev, R. Fleury, S. H. Mousavi, and A. Alu, Topologically robust sound propagation in an angular-momentum-biased graphene-like resonator lattice, Nature communications **6**, 8260 (2015).
[7] G. Ma, M. Xiao, and C. T. Chan, Topological phases in acoustic and mechanical systems, Nature Reviews Physics **1**, 281 (2019).
[8] S. Imhof, C. Berger, F. Bayer, J. Brehm, L. W. Molenkamp, T. Kiessling, F. Schindler, C. H. Lee,

M. Greiter, T. Neupert, and R. Thomale, Topolectrical-circuit realization of topological corner modes, Nature Physics **14**, 925 (2018).
[9] M. Hafezi, S. Mittal, J. Fan, A. Migdall, and J. M. Taylor, Imaging topological edge states in silicon photonics, Nature Photonics **7**, 1001 (2013).
[10] M. C. Rechtsman, J. M. Zeuner, Y. Plotnik, Y. Lumer, D. Podolsky, F. Dreisow, S. Nolte, M. Segev, and A. Szameit, Photonic Floquet topological insulators, Nature **496**, 196 (2013).
[11] M. Aidelsburger, M. Lohse, C. Schweizer, M. Atala, J. T. Barreiro, S. Nascimbène, N. R. Cooper, I. Bloch, and N. Goldman, Measuring the Chern number of Hofstadter bands with ultracold bosonic atoms, Nature Physics **11**, 162 (2015).
[12] Z. Wang, Y. Chong, J. D. Joannopoulos, and M. Soljačić, Observation of unidirectional backscattering-immune topological electromagnetic states, Nature **461**, 772 (2009).
[13] M. Atala, M. Aidelsburger, M. Lohse, J. T. Barreiro, B. Paredes, and I. Bloch, Observation of chiral currents with ultracold atoms in bosonic ladders, Nature Physics **10**, 588 (2014).
[14] K. v. Klitzing, G. Dorda, and M. Pepper, New method for high-accuracy determination of the fine-structure constant based on quantized hall resistance, Phys. Rev. Lett. **45**, 494 (1980).
[15] T. Ozawa and I. Carusotto, Anomalous and Quantum Hall Effects in Lossy Photonic Lattices, Phys. Rev. Lett. **112**, 133902 (2014).
[16] L. Yuan, A. Dutt, and S. Fan, Synthetic frequency dimensions in dynamically modulated ring resonators, APL Photonics **6**, 071102 (2021).
[17] T. Ozawa and H. M. Price, Topological quantum matter in synthetic dimensions, Nature Reviews Physics **1**, 349 (2019).
[18] A. Dutt, M. Minkov, Q. Lin, L. Yuan, D. A. B. Miller, and S. Fan, Experimental Demonstration of Dynamical Input Isolation in Nonadiabatically Modulated Photonic Cavities, ACS Photonics **6**, 162 (2019).
[19] C. Leefmans, A. Dutt, J. Williams, L. Yuan, M. Parto, F. Nori, S. Fan, and A. Marandi, Topological dissipation in a time-multiplexed photonic resonator network, Nat. Phys. **18**, 442 (2022).
[20] B. Bartlett, A. Dutt, and S. Fan, Deterministic photonic quantum computation in a synthetic time dimension, Optica **8**, 1515 (2021).
[21] E. Lustig, S. Weimann, Y. Plotnik, Y. Lumer, M. A. Bandres, A. Szameit, and M. Segev, Photonic topological insulator in synthetic dimensions, Nature **567**, 356 (2019).
[22] A. Dutt, Q. Lin, L. Yuan, M. Minkov, M. Xiao, and S. Fan, A single photonic cavity with two independent physical synthetic dimensions, Science **367**, 59 (2020).
[23] O. Boada, A. Celi, J. I. Latorre, and M. Lewenstein, Quantum Simulation of an Extra Dimension, Phys. Rev. Lett. **108**, 133001 (2012).
[24] B. K. Stuhl, H.-I. Lu, L. M. Aycock, D. Genkina, and I. B. Spielman, Visualizing edge states with an atomic Bose gas in the quantum Hall regime, Science **349**, 1514 (2015).
[25] M. Mancini, G. Pagano, G. Cappellini, L. Livi, M. Rider, J. Catani, C. Sias, P. Zoller, M. Inguscio, M. Dalmonte, and L. Fallani, Observation of chiral edge states with neutral fermions in synthetic Hall ribbons, Science **349**, 1510 (2015).
[26] B. Sundar, B. Gadway, and K. R. A. Hazzard, Synthetic dimensions in ultracold polar molecules, Scientific Reports **8**, 3422 (2018).
[27] X.-W. Luo, X. Zhou, C.-F. Li, J.-S. Xu, G.-C. Guo, and Z.-W. Zhou, Quantum simulation of 2D topological physics in a 1D array of optical cavities, Nature Communications **6**, 7704 (2015).
[28] S. K. Kanungo, J. D. Whalen, Y. Lu, M. Yuan, S. Dasgupta, F. B. Dunning, K. R. A. Hazzard, and T. C. Killian, Realizing topological edge states with Rydberg-atom synthetic dimensions, Nat Commun **13**, 972 (2022).
[29] M. Yang, H.-Q. Zhang, Y.-W. Liao, Z.-H. Liu, Z.-W. Zhou, X.-X. Zhou, J.-S. Xu, Y.-J. Han, C.-F. Li, and G.-C. Guo, Realization of exceptional points along a synthetic orbital angular momentum dimension, Science Advances **9**, eabp8943 (2023).
[30] Y. Hu, C. Reimer, A. Shams-Ansari, M. Zhang, and M. Loncar, Realization of high-dimensional frequency crystals in electro-optic microcombs, Optica **7**, 1189 (2020).
[31] L. Yuan, Y. Shi, and S. Fan, Photonic gauge potential in a system with a synthetic frequency dimension, Opt. Lett. **41**, 741 (2016).
[32] L. Yuan and S. Fan, Bloch oscillation and unidirectional translation of frequency in a dynamically modulated ring resonator, Optica **3**, 1014 (2016).
[33] K. Wang, A. Dutt, K. Y. Yang, C. C. Wojcik, J. Vučković, and S. Fan, Generating arbitrary topological windings of a non-Hermitian band, Science **371**, 1240 (2021).
[34] A. Senanian, L. G. Wright, P. F. Wade, H. K. Doyle, and P. L. McMahon, Programmable large-scale simulation of bosonic transport in optical synthetic frequency lattices, Nat. Phys. **19**, 1333 (2023).
[35] J. Wang, S. Paesani, Y. Ding, R. Santagati, P. Skrzypczyk, A. Salavrakos, J. Tura, R. Augusiak, L. Mančinska, D. Bacco, D. Bonneau, J. W. Silverstone, Q. Gong, A. Acín, K. Rottwitt, L. K. Oxenløwe, J. L. O'Brien, A. Laing, and M. G. Thompson, Multidimensional quantum entanglement with large-scale integrated optics, Science **360**, 285 (2018).
[36] A. Dutt, L. Yuan, K. Y. Yang, K. Wang, S. Buddhiraju, J. Vučković, and S. Fan, Creating boundaries along a synthetic frequency dimension, Nat Commun **13**, 3377 (2022).
[37] X. Lu, A. Rao, G. Moille, D. A. Westly, and K. Srinivasan, Universal frequency engineering tool for microcavity nonlinear optics: multiple selective mode splitting of whispering-gallery resonances, Photon. Res., PRJ **8**, 1676 (2020).
[38] R. J. C. Spreeuw, N. J. van Druten, M. W. Beijersbergen, E. R. Eliel, and J. P. Woerdman, Classical realization of a strongly driven two-level system, Phys. Rev. Lett. **65**, 2642 (1990).
[39] M. Zhang, C. Wang, Y. Hu, A. Shams-Ansari, T. Ren, S. Fan, and M. Lončar, Electronically programmable photonic molecule, Nature Photonics **13**, 36 (2018).
[40] I. Martin, G. Refael, and B. Halperin, Topological frequency conversion in strongly driven quantum systems, Phys. Rev. X **7**, 041008 (2017).
[41] E. Boyers, P. J. D. Crowley, A. Chandran, and A. O. Sushkov, Exploring 2d synthetic quantum hall physics

with a quasiperiodically driven qubit, Phys. Rev. Lett. **125**, 160505 (2020).
[42] D. Malz and A. Smith, Topological two-dimensional floquet lattice on a single superconducting qubit, Phys. Rev. Lett. **126**, 163602 (2021).
[43] H. Weyl, Z. Physik **56**, 330 (1929).
[44] X.-L. Qi, Y.-S. Wu, and S.-C. Zhang, Topological quantization of the spin Hall effect in two-dimensional paramagnetic semiconductors, Phys. Rev. B **74**, 085308 (2006).
[45] B. A. Bernevig, T. L. Hughes, and S.-C. Zhang, Quantum Spin Hall Effect and Topological Phase Transition in HgTe Quantum Wells, Science **314**, 1757 (2006).
[46] A. P. Schnyder, S. Ryu, A. Furusaki, and A. W. W. Ludwig, Classification of topological insulators and superconductors in three spatial dimensions, Phys. Rev. B **78**, 195125 (2008).
[47] A. Altland and M. R. Zirnbauer, Nonstandard symmetry classes in mesoscopic normal-superconducting hybrid structures, Phys. Rev. B **55**, 1142 (1997).
[48] F. Nathan, I. Martin, and G. Refael, Topological frequency conversion in a driven dissipative quantum cavity, Phys. Rev. B **99**, 094311 (2019).
[49] D. M. Long, P. J. Crowley, A. J. Kollár, and A. Chandran, Boosting the quantum state of a cavity with floquet driving, Physical Review Letters **128**, 183602 (2022).
[50] A. Dutt, M. Minkov, I. A. D. Williamson, and S. Fan, Higher-order topological insulators in synthetic dimensions, Light: Science & Applications **9**, 131 (2020).
[51] P. J. D. Crowley, I. Martin, and A. Chandran, Topological classification of quasiperiodically driven quantum systems, Physical Review B **99**, 10.1103/physrevb.99.064306 (2019).
[52] B. A. Bell, K. Wang, A. S. Solntsev, D. N. Neshev, A. A. Sukhorukov, and B. J. Eggleton, Spectral photonic lattices with complex long-range coupling, Optica **4**, 1433 (2017).
[53] K. Wang, B. A. Bell, A. S. Solntsev, D. N. Neshev, B. J. Eggleton, and A. A. Sukhorukov, Multidimensional synthetic chiral-tube lattices via nonlinear frequency conversion, Light: Science & Applications **9**, 132 (2020).
[54] S. V. Boriskina, Spectrally engineered photonic molecules as optical sensors with enhanced sensitivity: a proposal and numerical analysis, JOSA B **23**, 1565 (2006).
[55] Ó. B. Helgason, F. R. Arteaga-Sierra, Z. Ye, K. Twayana, P. A. Andrekson, M. Karlsson, and J. Schröder, Dissipative solitons in photonic molecules, Nature Photonics **15**, 305 (2021).
[56] Y. Zhang, M. Menotti, K. Tan, V. Vaidya, D. Mahler, L. Helt, L. Zatti, M. Liscidini, B. Morrison, and Z. Vernon, Squeezed light from a nanophotonic molecule, Nature communications **12**, 2233 (2021).
[57] M. A. Guidry, D. M. Lukin, K. Y. Yang, and J. Vučković, Multimode squeezing in soliton crystal microcombs, Optica **10**, 694 (2023).
[58] X. Jiang, Q. Lin, J. Rosenberg, K. Vahala, and O. Painter, High-q double-disk microcavities for cavity optomechanics, Opt. Express **17**, 20911 (2009).
[59] Y. Hara, T. Mukaiyama, K. Takeda, and M. Kuwata-Gonokami, Photonic molecule lasing, Optics letters **28**, 2437 (2003).
[60] H. Tian, J. Liu, A. Siddharth, R. N. Wang, T. Blésin, J. He, T. J. Kippenberg, and S. A. Bhave, Magnetic-free silicon nitride integrated optical isolator, Nat. Photon. **15**, 828 (2021).
[61] M. Zhang, C. Wang, R. Cheng, A. Shams-Ansari, and M. Lončar, Monolithic ultra-high-Q lithium niobate microring resonator, Optica, OPTICA **4**, 1536 (2017).
[62] R. Gao, N. Yao, J. Guan, L. Deng, J. Lin, M. Wang, L. Qiao, W. Fang, and Y. Cheng, Lithium niobate microring with ultra-high q factor above 10 8, Chinese Optics Letters **20**, 011902 (2022).
[63] M. Zhang, C. Wang, Y. Hu, A. Shams-Ansari, T. Ren, S. Fan, and M. Lončar, Electronically programmable photonic molecule, Nature Photonics **13**, 36 (2019).
[64] F. Yang, X. Fang, X. Chen, L. Zhu, F. Zhang, Z. Chen, and Y. Li, Monolithic thin film lithium niobate electro-optic modulator with over 110 ghz bandwidth, Chinese Optics Letters **20**, 022502 (2022).
[65] A. del Campo, Shortcuts to adiabaticity by counterdiabatic driving, Phys. Rev. Lett. **111**, 100502 (2013).
[66] G. Li, L. Wang, R. Ye, Y. Zheng, D.-W. Wang, X.-J. Liu, A. Dutt, L. Yuan, and X. Chen, Direct extraction of topological zak phase with the synthetic dimension, Light: Science & Applications **12**, 81 (2023).
[67] A. Dutt, M. Minkov, Q. Lin, L. Yuan, D. A. B. Miller, and S. Fan, Experimental band structure spectroscopy along a synthetic dimension, Nature Communications **10**, 3122 (2019).
[68] A. M. Turner, A. Vishwanath, and C. O. Head, Beyond band insulators: topology of semimetals and interacting phases, Topological Insulators **6**, 293 (2013).
[69] S.-Y. Xu, I. Belopolski, N. Alidoust, M. Neupane, G. Bian, C. Zhang, R. Sankar, G. Chang, Z. Yuan, C.-C. Lee, *et al.*, Discovery of a weyl fermion semimetal and topological fermi arcs, Science **349**, 613 (2015).
[70] G. B. Osterhoudt, L. K. Diebel, M. J. Gray, X. Yang, J. Stanco, X. Huang, B. Shen, N. Ni, P. J. Moll, Y. Ran, *et al.*, Colossal mid-infrared bulk photovoltaic effect in a type-i weyl semimetal, Nature materials **18**, 471 (2019).
[71] S. Vaidya, J. Noh, A. Cerjan, C. Jörg, G. von Freymann, and M. C. Rechtsman, Observation of a charge-2 photonic weyl point in the infrared, Phys. Rev. Lett. **125**, 253902 (2020).
[72] L. Yuan, Q. Lin, A. Zhang, M. Xiao, X. Chen, and S. Fan, Photonic Gauge Potential in One Cavity with Synthetic Frequency and Orbital Angular Momentum Dimensions, Physical Review Letters **122**, 083903 (2019).
[73] S. Buddhiraju, A. Dutt, M. Minkov, I. A. D. Williamson, and S. Fan, Arbitrary linear transformations for photons in the frequency synthetic dimension, Nature Communications **12**, 2401 (2021).
[74] T. Dubček, C. J. Kennedy, L. Lu, W. Ketterle, M. Soljačić, and H. Buljan, Weyl Points in Three-Dimensional Optical Lattices: Synthetic Magnetic Monopoles in Momentum Space, Phys. Rev. Lett. **114**, 225301 (2015).
[75] B. A. Bernevig, Topological insulators and topological superconductors, in *Topological Insulators and Topological Superconductors* (Princeton university press, 2013).
[76] K. Schwennicke and J. Yuen-Zhou, Enantioselective Topological Frequency Conversion, J. Phys. Chem. Lett. **13**, 2434 (2022).

DATA AVAILABILITY STATEMENT

The authors declare that the data supporting the findings of this study are available within the paper and its supplementary information files. The source data will be made available on zenodo.org upon publication.

Supplemental Materials: Quantized topological energy pumping and Weyl points in Floquet synthetic dimensions with a driven-dissipative photonic molecule

I. HALF-BHZ HAMILTONIAN FOR A PHOTONIC MOLECULE

Consider the two-resonator system with a Hamiltonian

$$H = \omega_0 \left(a_1^\dagger a_1 + a_2^\dagger a_2 \right) + \frac{\mu}{2} \left(a_1^\dagger a_2 + a_2^\dagger a_1 \right) + gV(t)(a_1^\dagger a_1 - a_2 a_2^\dagger) \tag{S1}$$

where a_1 and a_2 are the respective bosonic annihilation operators for the individual ring resonator modes at the resonance ω_0, with a coupling rate μ, and an electro-optic coupling coefficient g. Upon diagonalizing the time-independent terms, the Hamiltonian becomes

$$H = \omega_+ c_1^\dagger c_1 + \omega_- c_2^\dagger c_2 + gV(t)(c_1^\dagger c_2 + c_2^\dagger c_1) \tag{S2}$$

with $\omega_\pm = \omega_0 \pm \dfrac{\mu}{2}$ and $c_1 = \dfrac{1}{\sqrt{2}}\left(a_1 + a_2\right), c_2 = \dfrac{1}{\sqrt{2}}\left(a_1 - a_2\right)$. With a variable change, we can rotate out the $\omega_0 \left(c_1^\dagger c_1 + c_2^\dagger c_2 \right)$ term (within the single-photon subspace) and consider $\omega_\pm = \pm\dfrac{\mu}{2}$. We specify $V(t)$ to have a carrier tone ω_m with independent amplitude I-Q modulations and frequency modulation, giving us

$$H = \omega_+ c_1^\dagger c_1 + \omega_- c_2^\dagger c_2 + g\left[V_x(t)\cos\left(\omega_m t + \Delta(t)\right) + V_y(t)\sin\left(\omega_m t + \Delta(t)\right)\right]\left(c_1^\dagger c_2 + c_2^\dagger c_1\right) \tag{S3}$$

where $V_x(t)$, $V_y(t)$ and $\Delta(t)$ respectively denote the in-phase (I) amplitude, quadrature (Q) amplitude, and frequency modulations. We can define our spin-matrices to be

$$\begin{aligned}
\sigma_x &= \left(c_1^\dagger c_2 + c_2^\dagger c_1 \right) \\
\sigma_y &= -i\left(c_1^\dagger c_2 - c_2^\dagger c_1 \right) \\
\sigma_z &= \left(c_1^\dagger c_1 - c_2^\dagger c_2 \right)
\end{aligned}$$

in the single-photon subspace. These operators now form a Pauli group and obey the same commutation relations. In terms of these new spin operators, the Hamiltonian is

$$H = \frac{\mu}{2}\sigma_z + gV(t)\sigma_x = \frac{\mu}{2}\sigma_z + g\left[V_x(t)\cos\left\{\omega_m t + \Delta(t)\right\} + V_y(t)\sin\left\{\omega_m t + \Delta(t)\right\}\right]\sigma_x \tag{S4}$$

In the interaction picture, we can consider $U = \exp\left[i\sigma_z\{\omega_m t + \Delta(t)\}/2\right]$, and the dynamic Hamiltonian becomes

$$V_I(t) = \exp\left[i\sigma_z\{\omega_m t + \Delta(t)\}/2\right]\,\left(gV(t)\sigma_x\right)\exp\left[-i\sigma_z\{\omega_m t + \Delta(t)\}/2\right] = gV(t)\sum_{k=0}^{\infty}\frac{(i\omega_m t + \Delta(t))^k}{2^k k!}\left[\sigma_z, \sigma_x\right]_{(k)} \tag{S5}$$

where

$$\begin{aligned}
\left[A, B\right]_0 &= B \\
\left[A, B\right]_1 &= [A, B] \\
\left[A, B\right]_2 &= [A, [A, B]] \\
\left[A, B\right]_3 &= [A, [A, [A, B]]]
\end{aligned}$$

and so on. Since $[\sigma_z, \sigma_x] = 2i\sigma_y, [\sigma_z, \sigma_y] = -2i\sigma_x$,

$$\begin{aligned}
V_I(t) = gV(t)&\left[-\sum_k \frac{(-1)^k(\omega_m t + \Delta(t))^{(2k+1)}}{(2k+1)!}\sigma_y + \sum_k \frac{(-1)^k(\omega_m t + \Delta(t))^{2k}}{(2k)!}\sigma_x\right] \\
&= gV(t)\left[-\sin\{\omega_m t + \Delta(t)\}\sigma_y + \cos\{\omega_m t + \Delta(t)\}\sigma_x\right] \\
&= g\left[V_x(t)\cos\left\{\omega_m t + \Delta(t)\right\} + V_y(t)\sin\left\{\omega_m t + \Delta(t)\right\}\right]\left[-\sin\{\omega_m t + \Delta(t)\}\sigma_y + \cos\{\omega_m t + \Delta(t)\}\sigma_x\right]
\end{aligned} \tag{S6}$$

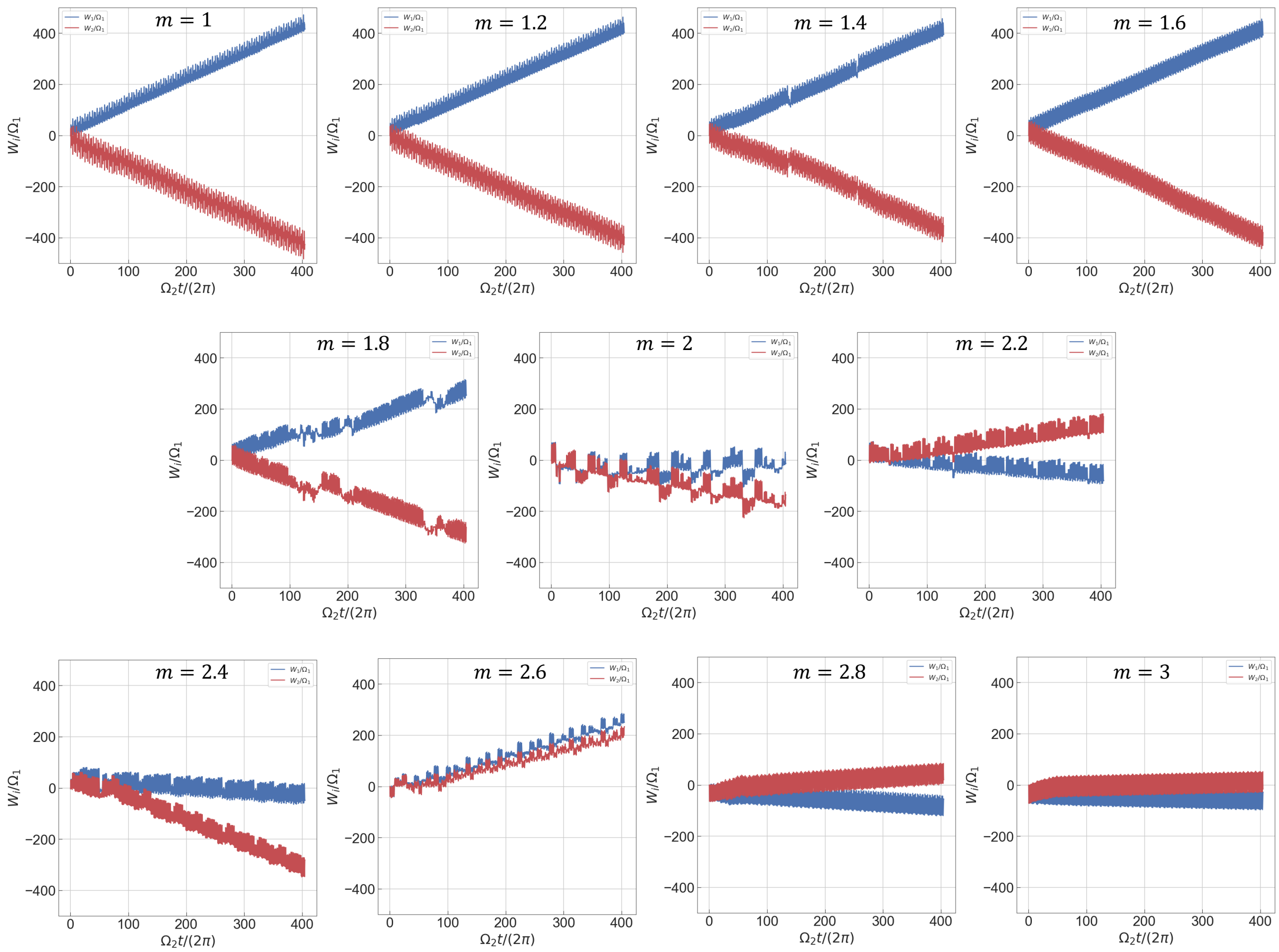

FIG. S1. Topological energy pumping for $\Omega_2/\Omega_1 = (1+\sqrt{5})/2$. We see a qualitative change in behavior around $m = 2$, indicative of the topological transition. We simulate this with $gV_0 = 40\Omega_1$ and $\gamma = 0.01\Omega_1/\pi$.

For $|gV_x(t)|, |gV_y(t)| \ll \omega_m$, we can expand and apply the rotating wave approximation to V_I, keeping only the slowly rotating terms.

$$\begin{aligned} V_I(t) &= g\left(e^{i(\omega_m t+\Delta(t))}\left(V_x(t) - iV_y(t)\right) + c.c.\right)\left(e^{i(\omega_m t+\Delta(t))}(\sigma_x + i\sigma_y)/2 + h.c.\right) \\ &\approx \frac{gV_x(t)}{2}\sigma_x + \frac{gV_y(t)}{2}\sigma_y \end{aligned} \tag{S7}$$

In this rotated frame, taking $\lambda(t) = d\Delta/dt$ and $\delta = \omega_m - \mu$, the Hamiltonian becomes,

$$\begin{aligned} \mathcal{H} &= UHU^\dagger + i\frac{\partial U}{\partial t}U^\dagger \\ &= -\frac{\delta + \lambda(t)}{2}\sigma_z + \frac{gV_x(t)}{2}\sigma_x + \frac{gV_y(t)}{2}\sigma_y \end{aligned} \tag{S8}$$

II. WEYL POINTS IN FLOQUET SYNTHETIC DIMENSIONS

Floquet synthetic dimensions allow for the direct simulation of k-space Hamiltonians by emulating their evolution with incommensurate drive phases. Thus, we can achieve Hamiltonians such as

$$\mathcal{H}(\mathbf{k}) = \Omega_R\{\sin(k_x)\sigma_x + \cos(k_y)\sigma_y + \cos(k_z)\sigma_z\} \tag{S9}$$

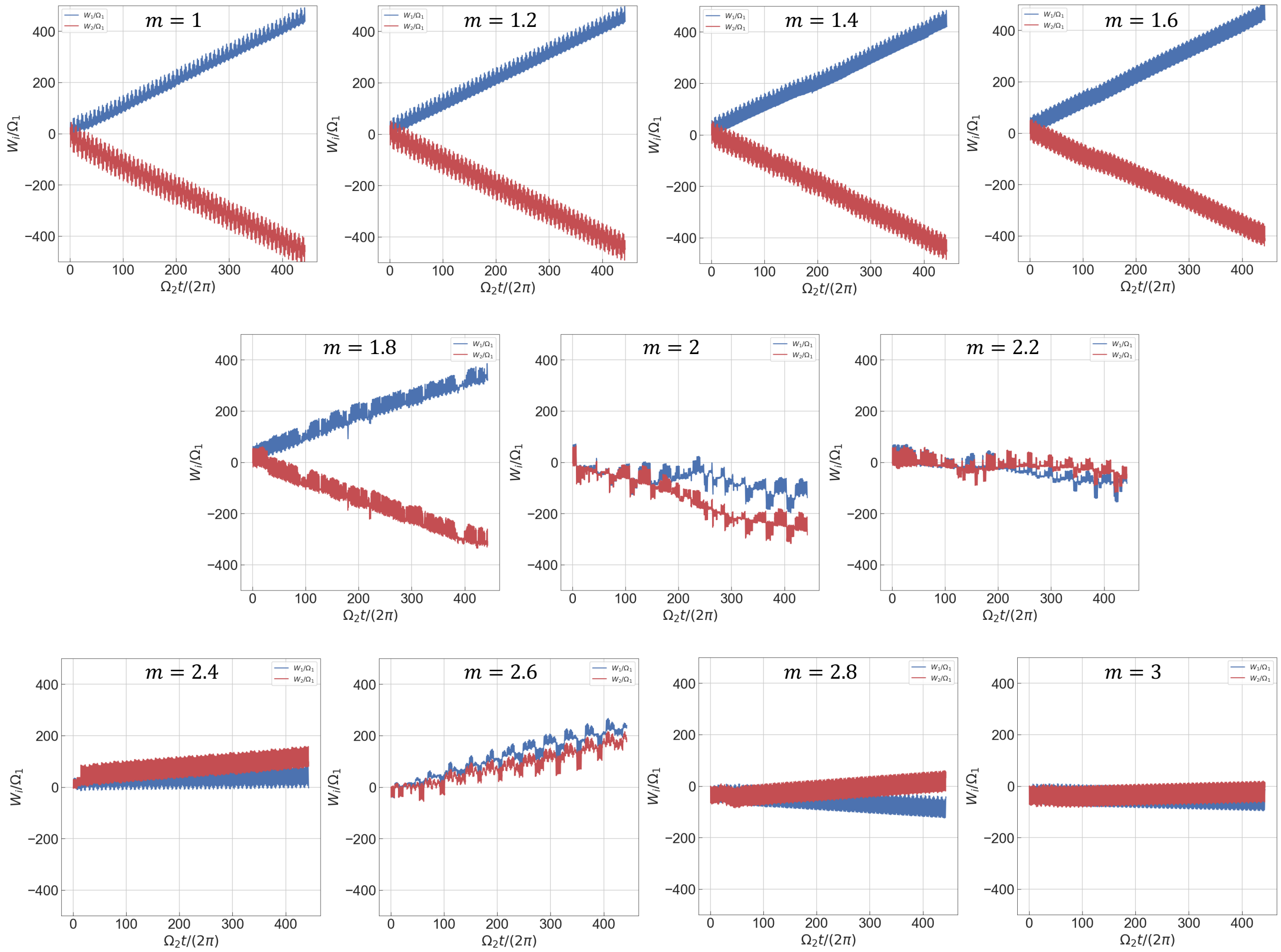

FIG. S2. Topological energy pumping for $\Omega_2/\Omega_1 = \sqrt{\pi}$. The transition persists for a different choice of irrational ratio. We simulate this with $gV_0 = 40\Omega_1$ and $\gamma = 0.01\Omega_1/\pi$.

by simply performing the substitutions, $\Omega_1 t + \phi_1 \to k_x$, $\Omega_2 t + \phi_2 \to k_y$ and $\Omega_3 t + \phi_3 \to k_z$. The linear evolution of these phases also emulates the effect of a synthetic electric field, which naturally allows us to study charge transport effects in these systems. We now study this Hamiltonian and its topological effects in detail. The gauge-invariant Berry curvature of this system can be written as

$$\mathbf{B}(\mathbf{k}) = \mathrm{Im}\left[\frac{\langle n(\mathbf{k})| \{\nabla_{\mathbf{k}}\mathcal{H}(\mathbf{k})\} |m(\mathbf{k})\rangle \times \langle m(\mathbf{k})| \{\nabla_{\mathbf{k}}\mathcal{H}(\mathbf{k})\} |n(\mathbf{k})\rangle}{(E_m - E_n)^2}\right] \tag{S10}$$

We evaluate $\nabla_{\mathbf{k}}\mathcal{H}(\mathbf{k})$ to be

$$\nabla_{\mathbf{k}}\mathcal{H}(\mathbf{k}) = \Omega_R[\hat{k}_x \cos(k_x)\sigma_x - \hat{k}_y \sin(k_y)\sigma_y - \hat{k}_z \sin(k_z)\sigma_z]$$

where $\hat{k}_i$ $(i = x, y, z)$ is the unit vector in the Floquet momentum space. Another important quantity to calculate are the eigenvalues and eigenvectors of the Hamiltonian as functions of $\mathbf{k}$. Using the properties of spin-1/2 Hamiltonians, we get

$$\begin{aligned} E_m &= \Omega_R\sqrt{\sin^2 k_x + \cos^2 k_y + \cos^2 k_z} = -E_n = E \\ \rho_m &= |m\rangle\langle m| = \frac{1}{2}\left(\mathbb{I} + \frac{\mathcal{H}(\mathbf{k})}{E}\right) \\ \rho_n &= |n\rangle\langle n| = \frac{1}{2}\left(\mathbb{I} - \frac{\mathcal{H}(\mathbf{k})}{E}\right) \end{aligned} \tag{S11}$$

965 Substituting these into Eq. S10 and using properties of Pauli matrices,

$$
\begin{aligned}
\mathbf{B}(\mathbf{k}) &= \frac{\Omega_R^2}{4E^2}\mathrm{Im}\big[\hat{k}_x \sin(k_y)\sin(k_z)\langle n|\,\sigma_y\rho_m\sigma_z - \sigma_z\rho_m\sigma_y\,|n\rangle - \hat{k}_y\cos(k_x)\sin(k_z)\langle n|\,\sigma_z\rho_m\sigma_x - \sigma_x\rho_m\sigma_z\,|n\rangle \\
&\quad -\hat{k}_z\cos(k_x)\sin(k_y)\langle n|\,\sigma_x\rho_m\sigma_y - \sigma_y\rho_m\sigma_x\,|n\rangle\big] \\
&= \frac{\Omega_R^2}{8E^2}\mathrm{Im}\Bigg[\hat{k}_x\sin(k_y)\sin(k_z)\langle n|\left([\sigma_y,\sigma_z] - 2i\sin(k_x)\frac{\Omega_R\mathbb{I}}{E}\right)|n\rangle \\
&\quad -\hat{k}_y\cos(k_x)\sin(k_z)\langle n|\left([\sigma_z,\sigma_x] - 2i\cos(k_y)\frac{\Omega_R\mathbb{I}}{E}\right)|n\rangle \\
&\quad -\hat{k}_z\cos(k_x)\sin(k_y)\langle n|\left([\sigma_x,\sigma_y] - 2i\cos(k_z)\frac{\Omega_R\mathbb{I}}{E}\right)|n\rangle\Bigg] \\
&= \frac{\Omega_R^2}{4E^2}\Bigg[\hat{k}_x\sin(k_y)\sin(k_z)\left(\langle n|\,\sigma_x\,|n\rangle - \frac{\Omega_R\sin(k_x)}{E}\right) - \hat{k}_y\cos(k_x)\sin(k_z)\left(\langle n|\,\sigma_y\,|n\rangle - \frac{\Omega_R\cos(k_y)}{E}\right) \\
&\quad -\hat{k}_z\cos(k_x)\sin(k_y)\left(\langle n|\,\sigma_z\,|n\rangle - \frac{\Omega_R\cos(k_z)}{E}\right)\Bigg]
\end{aligned} \tag{S12}
$$

966 This is Eq. 13 in the main text, and the Berry curvature in this form can be measured experimentally, when adiabaticity
967 is maintained. Simplifying further, we get

$$
\begin{aligned}
\mathbf{B}(\mathbf{k}) &= \frac{\Omega_R^2}{4E^2}\Bigg[\hat{k}_x\sin(k_y)\sin(k_z)\left(\mathrm{Tr}\{\rho_n\sigma_x\} - \frac{\Omega_R\sin(k_x)}{E}\right) - \hat{k}_y\cos(k_x)\sin(k_z)\left(\mathrm{Tr}\{\rho_n\sigma_y\} - \frac{\Omega_R\cos(k_y)}{E}\right) \\
&\quad -\hat{k}_z\cos(k_x)\sin(k_y)\left(\mathrm{Tr}\{\rho_n\sigma_z\} - \frac{\Omega_R\cos(k_z)}{E}\right)\Bigg] \\
&= \frac{-\hat{k}_x\sin(k_x)\sin(k_y)\sin(k_z)\sigma_x + \hat{k}_y\cos(k_x)\cos(k_y)\sin(k_z)\sigma_y + \hat{k}_z\cos(k_x)\sin(k_y)\cos(k_z)\sigma_z}{2\left(\sin^2 k_x + \cos^2 k_y + \cos^2 k_z\right)^{3/2}}
\end{aligned} \tag{S13}
$$

968 where the final closed form expression for the Berry curvature comes from substituting Eq. S11, containing the
969 expression for ρ_n. We then plot this in the main text to see the monopole behavior of Weyl points. The curvature at
970 the Weyl point diverges, and integrating around this singularity leads to the quantized Chern number that characterizes
971 the topological effects of this system.

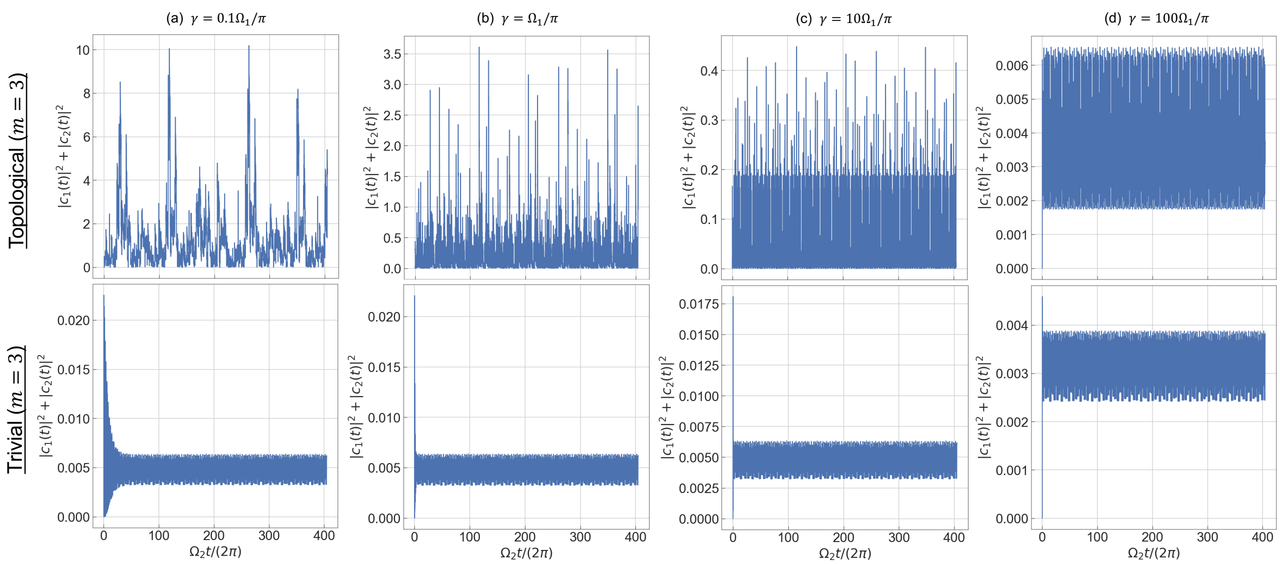

FIG. S3. Total power in the photonic molecule for different photon loss rates. The driven-dissipative system reaches a quasi-steady state, with the intra-cavity power displaying oscillations, but not fully decaying or diverging.

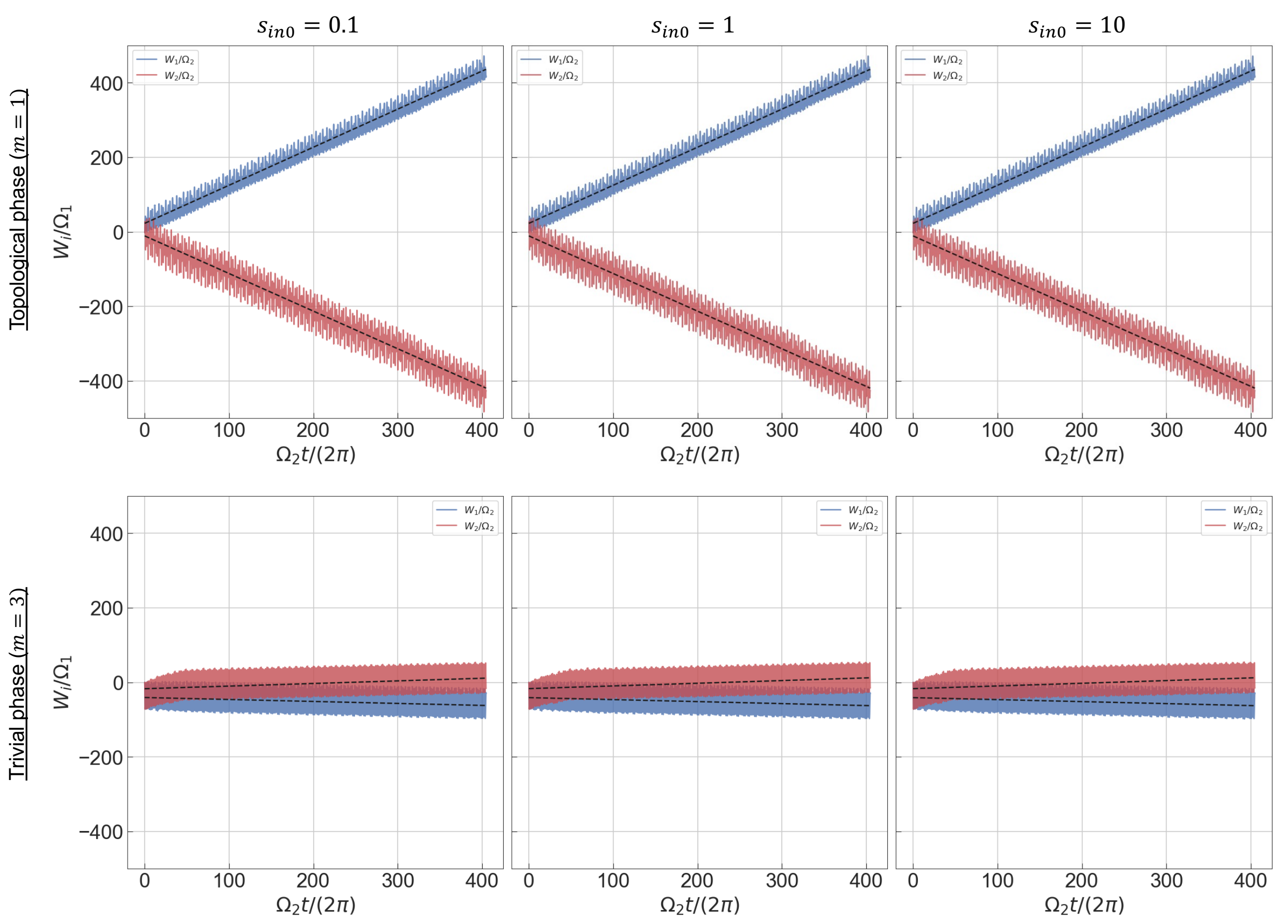

FIG. S4. Topological energy pumping for different amplitudes of external laser drive $s_{in}(t)$. We see that there is no change in the pumping behaviour, as the normalization by the total power in both supermodes accounts for this variation.

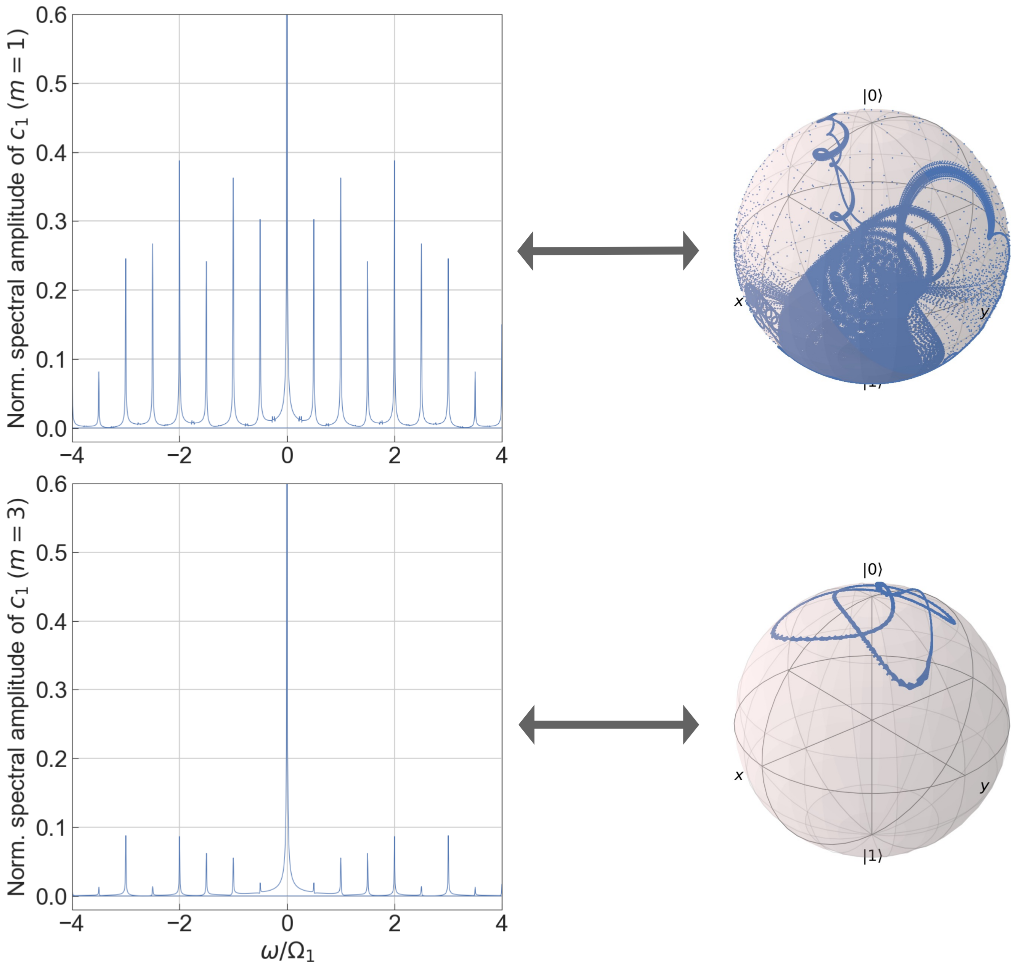

FIG. S5. Spectral amplitudes and Bloch sphere trajectories for the commensurate frequency case, in the topological and trivial phases ($\Omega_2/\Omega_1 = 1.5$). The trajectories on the Bloch sphere correspond to periodic orbits, which show a corresponding spectrum of equally-spaced harmonics in the frequency domain and do not cover the full Bloch sphere. The time-evolution in this case is visualized in SI videos 3 & 4. Importantly, note the absence of a continuous noise floor in both cases compared to main text Fig. 3a in the topological regime for incommensurate drive frequencies. The absence of a continuous noise floor and the presence of equally spaced harmonics in both regimes signifies the lack of a topological phase transition for the commensurate frequency case.

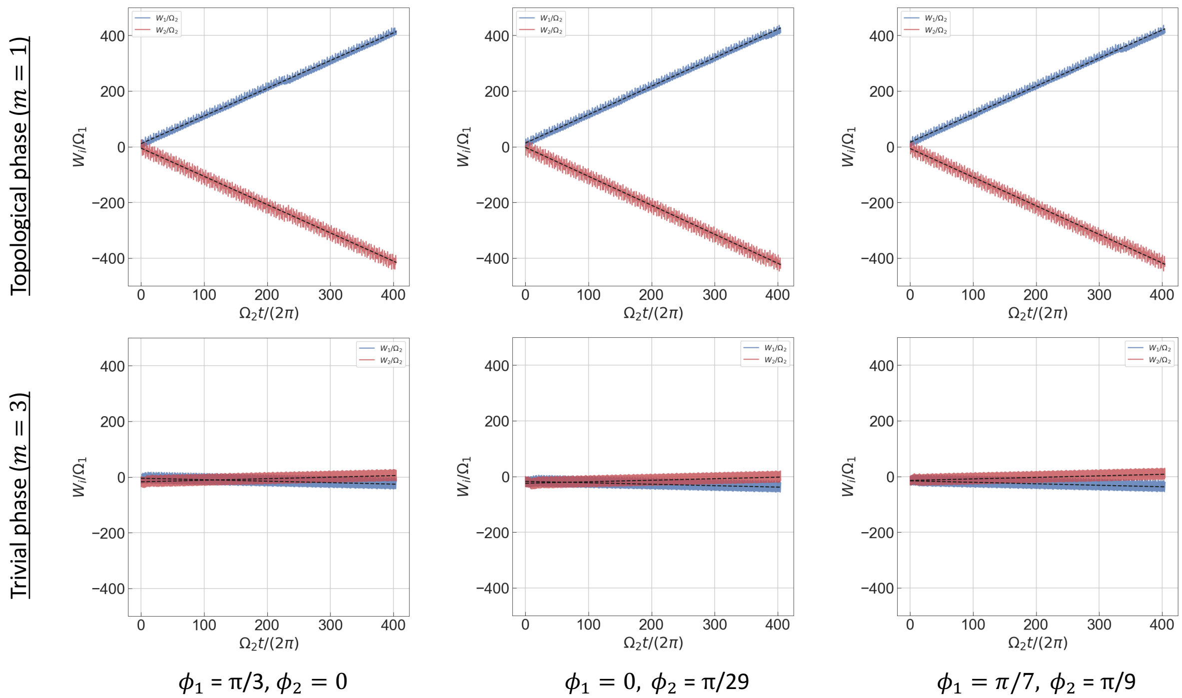

FIG. S6. Simulations for the pumping with different initial phases for the drives, i.e., different values of (k_{x0}, k_{y0}) in the synthetic Floquet lattice. Due to the quasi-steady state nature of our protocol, we see no major difference in the simulated slopes, except for small kinks at points where the trajectory could be passing through the Berry curvature singularity at the origin due to the external drive.

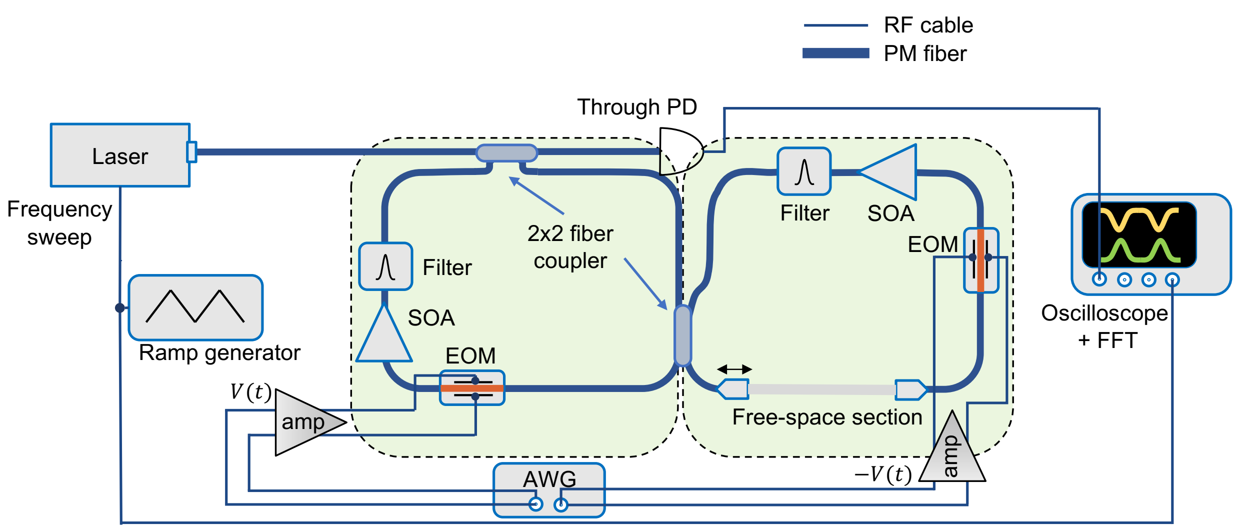

FIG. S7. Experimental Schematic of the fiber-optic photonic molecule setup. The 2x2 fiber couplers split a portion of the light from the laser and couple the two rings together, producing symmetric and anti-symmetric supermodes at all the resonances when the lengths are exactly matched, which is ensured by the movable free-space section. The rings contain electro-optic modulators (EOMs) to couple the supermodes, semiconductor optical amplifiers (SOAs) to account for the losses, and filters to remove any ASE (amplified spontaneous emission) noise after the SOAs. The EOMs are driven by AWGs programmed with the amplitude I-Q and phase modulation required, and are calibrated to opposite polarities in each EOM to ensure coupling between the supermodes. The laser frequency is slowly swept by the ramp generator. Data is collected at the through port with a photodetector connected to the oscilloscope.

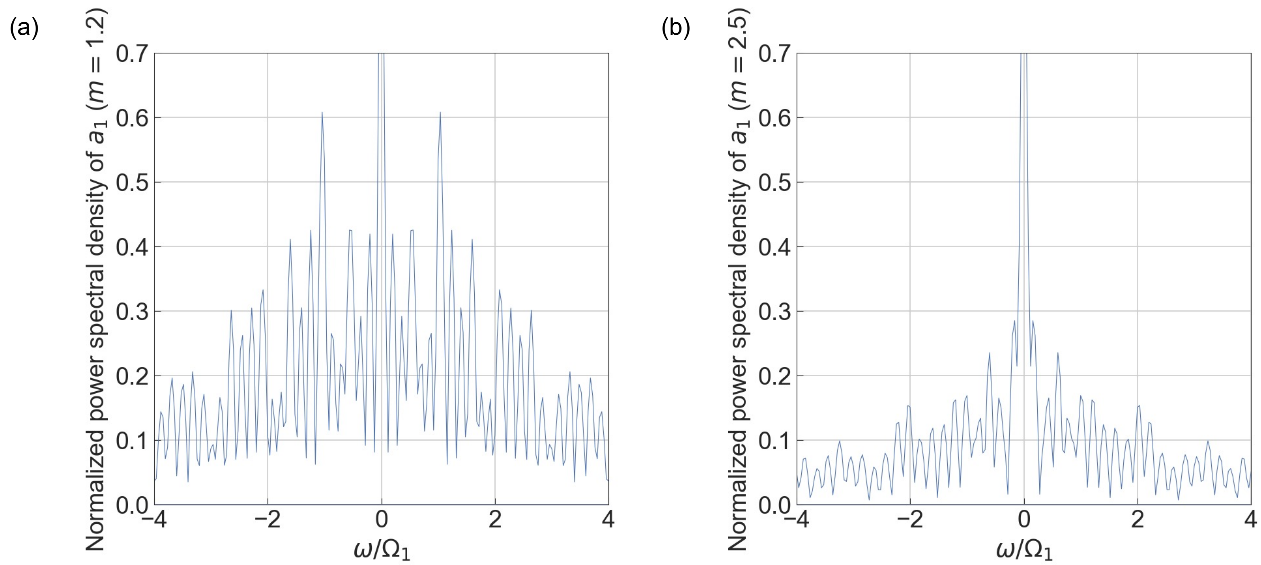

FIG. S8. Simulation of Power Spectral Densities in the (a) topological and (b) trivial regimes, in accordance with the experimental parameters for the data in Fig. 4(c). The simulations show very good agreement with the experimental data, showing robust signatures of topology even in a high-loss regime. The difference in magnitudes of the PSD between simulation and experiment arises from the large DC component in the measurement, which also measures the laser output at the through port of the rings.